The Interstellar Magnetic Field Close to the Sun II.

P. C. Frisch

Dept. Astronomy and Astrophysics, University of Chicago, Chicago, IL 60637

B-G Andersson

SOFIA, USRA

A. Berdyugin and V. Piirola

Finnish Centre for Astronomy with ESO, University of Turku, Finland

R. DeMajistre

The Johns Hopkins University Applied Physics Laboratory, Laurel, MD

H. O. Funsten

Los Alamos National Laboratory, Los Alamos, NM

A. M. Magalhaes and D. B. Seriacopi

Inst. de Astronomia, Geofisica e Ciencias Atmosfericas, Universidade de Sao Paulo, Brazil

D. J. McComas[1]

Southwest Research Institute, San Antonio, TX

N. A. Schwadron

Space Science Center, University of New Hampshire

J. D. Slavin

Harvard-Smithsonian Center for Astrophysics, Cambridge, MA

S. J. Wiktorowicz

Dept. Astronomy, University of California at Santa Cruz, Santa Cruz, CA

---

[1]also University of Texas, San Antonio, TX

ABSTRACT

The magnetic field in the local interstellar medium (ISM) provides a key indicator of the galactic environment of the Sun and influences the shape of the heliosphere. We have studied the interstellar magnetic field (ISMF) in the solar vicinity using polarized starlight for stars within 40 parsecs of the Sun and $90°$ of the heliosphere nose. In Frisch et al. (2010, Paper I) we developed a method for determining the local ISMF direction by finding the best match to a group of interstellar polarization position angles obtained towards nearby stars, based on the assumption that the polarization is parallel to the ISMF. In this paper we extend the analysis by utilizing weighted fits to the position angles and by including new observations acquired for this study. We find that the local ISMF is pointed towards the galactic coordinates $\ell,b= 47° \pm 20°, 25° \pm 20°$. This direction is close to the direction of the ISMF that shapes the heliosphere, $\ell,b= 33° \pm 4°, 55° \pm 4°$, as traced by the center of the "Ribbon" of energetic neutral atoms discovered by the Interstellar Boundary Explorer (IBEX) mission. Both the magnetic field direction and the kinematics of the local ISM are consistent with a scenario where the local ISM is a fragment of the Loop I superbubble. A nearby ordered component of the local ISMF has been identified, in the region $\ell \approx 0° \rightarrow 80°$ and $b \approx 0° \rightarrow 30°$, where PlanetPol data show a distance-dependent increase of polarization strength. The ordered component extends to within 8 parsecs of the Sun and implies a weak curvature in the nearby ISMF of $\sim 0.25°$ per parsec. This conclusion is conditioned on the small sample of stars available for defining this rotation. Variations from the ordered component suggest a turbulent component of $\sim 23°$. The ordered component and standard relations between polarization, color excess, and H° column density predict a reasonable increase of N(H) with distance in the local ISM. The similarity of the ISMF directions traced by the polarizations, the IBEX Ribbon, and pulsars inside the Local Bubble in the third galactic quadrant suggest that the ISMF is relatively uniform over spatial scales of 8–200 parsecs and is more similar to interarm than spiral-arm magnetic fields. The ISMF direction from the polarization data is also consistent with small-scale spatial asymmetries detected in GeV-TeV cosmic rays with a galactic origin. The peculiar geometrical relation found earlier between the cosmic microwave background dipole moment, the heliosphere nose, and the ISMF direction, is supported by this study. The interstellar radiation field at ~ 975 Å does not appear to play a role in grain alignment for the low density ISM studied here.

Subject headings: ISM: magnetic field, clouds, solar system: general, Galaxy: solar neighborhood, cosmology: cosmic microwave background

1. Introduction

The characteristics of the interstellar magnetic field (ISMF) in the warm, low density, partially ionized interstellar gas near the Sun are difficult to study. A new diagnostic of the magnetic field in the Local Interstellar Cloud (LIC) surrounding the heliosphere is provided by the giant arc, or 'Ribbon', of energetic neutral atoms (ENAs) discovered by the Interstellar Boundary Explorer (IBEX) spacecraft (McComas et al. 2009, 2011). ENAs are formed by charge-exchange between interstellar neutral hydrogen atoms and the solar wind and other heliospheric ions. The ENA Ribbon is observed towards sightlines that are perpendicular to the ISMF direction as it drapes over the heliosphere, and is superimposed on a distributed ENA flux that traces the global heliosphere (Appendix A provides additional information on the Ribbon and Ribbon models). In Frisch et al. (2010a, Paper I) we showed that the measurements of interstellar polarization towards nearby stars yields a best-fit ISMF direction that is close to the field direction obtained from the IBEX Ribbon. In this paper, we further study the connection between the magnetic field sampled by the IBEX Ribbon and the magnetic field in the local ISM.

Starlight polarized by magnetically aligned dust grains in the ISM shows that the magnetic field in our galactic neighborhood has two large-scale components, a uniform field parallel to the galactic plane that is directed towards $\ell \sim 82.8°$[1] and extends beyond a kiloparsec, and a giant magnetic structure, Loop I, that is within 100 pc and dominates the northern sky and probably reaches to the solar location. The ISMF of Loop I is traced by optical polarizations (Mathewson & Ford 1970; Heiles 1976; Santos et al. 2011; Berdyugin et al. 2011), the polarized radio continuum (Berkhuijsen 1973; Wolleben 2007), and Faraday rotation measures (Taylor et al. 2009; Mao et al. 2010). It is a superbubble formed by stellar winds and supernova in the Sco-Cen Association during the past ~ 15 Myrs (e.g. de Geus 1992; Frisch 1995, 1996; Heiles 1998a, 2009). The interstellar magnetic field is swept up during superbubble expansion, creating a magnetic bubble that persists through the late stages of the bubble evolution (Tilley et al. 2006). Optical polarization and reddening data show that the eastern parts of Loop I, $\ell = 3° - 60°$, $b > 0°$, are within 60–80 parsecs of the Sun (Santos et al. 2011; Frisch et al. 2011). If Loop I is a spherical feature, the ISMF near the Sun should be associated with the Loop I superbubble (e.g. Frisch 1990; Heiles 1998b,a). The magnetic structure of Loop I provides a framework for understanding the magnetic field in the local ISM and the relation between the galactic magnetic field and the magnetic field that shapes the heliosphere.

In this paper we use high-sensitivity observations of the polarization toward nearby stars as a tool for determining the direction of the ISMF near the Sun, within ~ 40 parsecs. This study

---

[1] In this paper, galactic coordinates are denoted by ℓ, b, and ecliptic coordinates by λ, β. Plots in ecliptic coordinates are labeled as such.

builds on our earlier study (Paper I) which presents a new method for determining the ISMF direction, based on testing for the best match between polarization position angles and the ISMF, where we found that the best-fit local ISMF direction in the galactic hemisphere regions agrees, to within the uncertainties, with the ISMF direction defined by the center of the IBEX Ribbon arc. Our new study differs from the first study in that the method is broadened to include weighted fits (§2),which is possible because of the inclusion of new data (§3). The best-fit ISMF direction found from both unweighted fits (§4.1) and weighted fits (§4.2) is close to the direction of the ISMF shaping the heliosphere (§5.1). We also look closely at the PlanetPol data (Bailey et al. 2010, §5.3) and use the upper envelope of the polarization-distance curve (§5.3.1, Appendix C) to show that there is an ordered component in the local ISMF with a direction that varies weakly with distance and extends to within 8 parsecs of the Sun (§5.3.2). The ordered component provides information on magnetic turbulence. An anti-correlation of polarization with radiation fluxes suggests ineffective radiative torques (§5.3.3, Appendix D). The best-fit ISMF direction is compared with the field direction derived from the IBEX Ribbon, and the relation between the LIC and G-clouds (§5.1). For our new ISMF direction and the new IBEX heliosphere nose direction, the symmetry of the cosmic microwave background (CMB) dipole moment with respect to the heliosphere nose direction is still apparent (§5.3.4). The similar directions of the ISMF over scales of several hundred parsecs suggests an interarm-type field (§5.4.1). The local ISMF direction also appears to affect anisotropies observed in GeV–TeV galactic cosmic rays (§5.4.2). Results are summarized in §6.

2. Method of finding the best-fit ISMF direction

Optical polarization is an important probe of the direction of the ISMF in interstellar clouds, both over large spatial scales (Mathewson & Ford 1970) and the very local ISM (Tinbergen 1982; Frisch 1990; Frisch et al. 2010a). The observed polarization from aligned grains depends on the total column of dust and the grain size distribution (Mathis 1986), the fraction of asymmetrical dust grains and alignment efficiency of the grains (Whittet et al. 2008), and the projection of the magnetic field onto the sky. The axis of lowest average grain opacity is parallel to the ISMF direction (Davis & Greenstein 1951; Martin 1971; Roberge 2004; Lazarian 2007). [2] Polarization is a pseudo-vector entity (always in the range $0° - 180°$), and in denser regions radiative transfer effects can influence the observed polarization both due to turbulence in the probed medium (Jones, Dickey & Klebe 1992; Ostriker, Stone & Gammie, 2001), and due to the influence of foreground

---

[2]Leverett Davis provided the first viable model for the relation between the ISMF and starlight polarization, and also first proposed the existence of the solar wind cavity in the ISM, now known as the heliosphere. He proposed a solar wind cavity of radius ~ 200 AU partly out of the necessity of excluding the interstellar magnetic field from the solar system (Davis 1955).

depolarizing screens (Andersson & Potter 2006; Andersson 2012). ISM within 10 parsecs has low average ISM densities, $N(\mathrm{H}) \lesssim 10^{18}$ cm^{-2} and $< n > \sim 0.1$ cm^{-3}, suggesting there is very little nearby dust. Therefore depolarizing foreground screens and collisional disruption of grain alignment are less likely locally compared to distant dense cloud regions. This low density ISM is partially ionized (Frisch et al. 2011) so that gas and the ISMF will be tightly coupled.

Two properties of polarized starlight could in principle be exploited to obtain the ISMF direction causing the polarization: the position angle of the polarizations, which are measured with respect to a great circle meridian and increase positively to the east, and the polarization strengths that reach a maximum for sightlines perpendicular to the ISMF for a uniform medium. The drawbacks with using polarization strengths to determine the ISMF direction are that polarization varies with the dust column density of the sightline, and polarizations are weaker near the magnetic pole where the statistical significance of detections will be lower. Polarization directions are insensitive to the dust column density, but sensitive to magnetic turbulence that could distort the field over either small or large scales.

Paper I introduces a new method for determining the ISMF direction based on finding the best fit to an ensemble of polarization position angles. The analysis makes the assumption that the polarization position angle is parallel to the direction of the interstellar magnetic field (Roberge 2004). This assumption is justified for the diffuse clouds in Loop I, where the field directions determined from optical polarization data and synchrotron emission in high-latitude regions agree (Spoelstra 1972). The ensemble of data used in the analysis are chosen to meet a set of selection criteria. These data and the criteria are discussed in the following section (§3). All measurements meeting the criteria are used in the analysis, including multiple measurements of the same star by different observers.

The ISMF direction is derived by assuming that a single large-scale ISMF close to the Sun is aligning the grains, so that the polarization direction would then be parallel to a great-circle meridian of the "true" magnetic field direction. The best-fit ISMF is calculated to be the direction that corresponds to the minimum value of:

$$F_{\mathrm{i}} = F(B_{\mathrm{i}}) = \mathrm{N}^{-1} \sum_{\mathrm{n}=1}^{\mathrm{N}} \left| \frac{\sin(\theta_{\mathrm{n}}(B_{\mathrm{i}}))}{G_{\mathrm{n}}} \right| \tag{1}$$

where $\theta_{\mathrm{n}}(B_{\mathrm{i}})$ is the polarization position angle PA_{n} for star n, calculated with respect to the $\mathrm{i^{th}}$ possible interstellar magnetic field direction B_{i}, and where the sum is over N stars. G_{n} is the weighting factor for each star *n* based on the measurement uncertainties of the polarization position angle for that star. A grid resolution of $1°$ in longitude and latitude is used for the spacing of B_{i} values. An alternate approach to find the best-fit field direction $B_{\mathrm{i=best}}$ that maximizes the cosecants, i.e. maximize $\overline{|G_{\mathrm{n}}/sin(\theta_{\mathrm{n}}(B_{\mathrm{i}})|}$, generated numerical glitches related to dividing by zero, and is not used.

Paper I calculated the ISMF direction with the weighting factor G_n=1. Statistical weights were ignored since the northern hemisphere data included a large number of recent high-sensitivity data collected at ppm accuracy, while the southern hemisphere data were dominated by data collected in the 1970's that are less sensitive ($1\sigma >$60 ppm, §3). Weighting data points by the uncertainties yielded a magnetic field direction biased by the difference in uncertainties in the two hemispheres. The best-fit ISMF direction from Paper I is listed in Table 1. In this paper, new data (§3) are added and the unweighted fit is recalculated (§4.1).

New high-precision polarization data make it possible to evaluate the best-fit ISMF direction by utilizing all of the position angles in the sample, but weighting individual values according to their statistical significance. By combining data based on weighted values, the emphasis is implicitly placed on the ISMF field in the distant portions of the sampled ISM, where polarizations may be stronger relative to the measurement errors (depending on the patchiness of the ISM, §5.3). The probability distribution for position angles does not have a normal distribution for weak polarizations, $P/dP<$ 6. The weighting function is based on the results of Naghizadeh-Khouei & Clarke (1993a) that give the probability distribution for the position angle of linear polarization. For true polarization p_o with a measurement uncertainty of σ, and the true position angle in equatorial coordinates θ_o, the probability $G_n(\theta_{obs};\ \theta_o, P_o)$ of observing a position angle θ_{obs} (which will be $0°$ for the "true" value of a perfectly aligned PA) is:

$$G_n(\theta_{obs};\ \theta_o, P_o)\ =\ \frac{1}{\sqrt{\pi}}\ \{\frac{1}{\sqrt{\pi}} + \eta_o \exp(\eta_o^2)\, [1 + \mathrm{erf}(\eta_o)]\}\exp(-\frac{\mathrm{P}_o^2}{2}) \qquad (2)$$

where $\eta_o\ =\ \frac{P_o}{\sqrt{2}} \cos [2(\theta_{obs} - \theta_o)]$ and $P_o = \frac{P_o}{\sigma}$, and the function $erf(z)$ is the Gaussian error function $erf(Z)\ =\ \frac{2}{\sqrt{\pi}} \int_0^Z exp(-t^2)\, dt$. The goal is then to choose a procedure that maximizes the contributions of high-significance (e.g. high G_n) measurements, and minimizes the contributions from data points with large values of $\sin(\theta_{n,j})$. When $B_{i=best}$ is calculated using weighted fits (§4.2), the function G_n in eqn. 2 is adopted as the weighting factor for each star n in eqn. 1.

3. Polarization data used in study

The Local Bubble void appears as an absence of both interstellar gas and dust within ~ 70 parsecs, particularly in the third and fourth galactic quadrants. Figure 1 shows the distribution of interstellar dust within 100 pc, as traced by color excess E(B–V).[3] The interior of the Loop I superbubble appears as a void in the distribution of interstellar dust within 100 parsecs in the fourth

---

[3]Stars with δV $\geq$ 0.06 mag, according to the Hipparcos variability index H6, are omitted.

galactic quadrant ($\ell > 270°$). Models of Loop I as a spherical object place the Sun in or close to the rim of the shell (§5.2). This combination of properties is the basis for selecting polarized stars for this analysis within 90° of the heliosphere nose and 40 parsecs of the Sun. The heliosphere nose is remarkably close to the direction of the galactic center. IBEX-LO measurements of the 23.2 ± 0.3 km s^{-1} flow of interstellar He^o through the heliosphere provide the nose direction of $\ell = 5.25°\pm0.24°$, $b = 12.03°\pm0.51°$ (McComas et al. 2012). Most interstellar gas within 40 parsecs is also clumped within 20 parsecs of the Sun, as shown by interstellar H^o and D^o (Figure 2) and the fact that the average number of interstellar Fe$^+$, Ca$^+$, and Mg$^+$ velocity components is distant-independent for stars within 30 parsecs, and rises only slightly ($\sim 20\%$) for stars that are 30–40 parsecs (Frisch et al. 2011). This spatial interval provides for a well-defined region for study, accepts most stars in the region of Tinbergen's original "patch" of nearby polarization (Tinbergen 1982, Paper I), includes the region where PlanetPol (Bailey et al. 2010) obtained very high sensitivity polarization data (§3), and includes nearby stars observed towards Loop I by Santos et al. (2011).

These data show that the polarizations in the southern galactic hemisphere tend to be larger than polarizations in the northern galactic hemisphere. For the special case where the star sample is restricted to stars meeting the spatial and spectral criteria above, and to recent higher precision data, then the polarizations of southern stars with $P/dP > 2.5$, are $0.024\% \pm 0.017\%$, while for northern stars they are $0.003\% \pm 0.005\%$. Whether this difference, originally noted by Tinbergen (1982), is accurate will require additional high-sensitivity data (where P/dP gives the polarization strength divided by the 1σ uncertainty of the polarization).

New polarization measurements were also collected for this study using telescopes of the Laboratorio Nacional de Astropfisica (LNA) in Brazil and the Nordic Optical telescope (NOT) on the island of La Palma in the Canary Islands. The LNA data were acquired with the CCD polarimeter (Magalhaes et al. 1996) on the 0.6m telescope at Pico de Dios, during the months of June 2008, August 2010, September 2010, and May 2011. The NOT data were acquired using the TurPol polarimeter (Piirola 1973; Butters et al. 2009) on the 2.52m telescope on the island of La Palma in the Canary Islands during June 2010. Optical polarimetry is a differential measurement and good observing conditions are not as critical as for high accuracy photometry. ISM polarization data also sample a relatively constant polarization source, allowing repeated observations over different days or from different sites to maximize sensitivity and minimize systematic uncertainties. These new data are listed in Table 2. The columns in this table are HD number, galactic longitude and latitude, star distance, the polarization in units of 10^{-5}, and the polarization position in the equatorial coordinate system. The last column gives the observatory where the data were acquired.

The CCD imaging polarimeter at Pico dos Dias provided polarizations in the B-band. The instrument acquires CCD images of the orthogonal polarizations, in sets of 8 waveplate positions,

with several images at each plate position. In the case of constant polarizations such as interstellar polarizations, individual observations can be combined to reduce uncertainties. Stars brighter than ~ 7 mag were observed through a neutral density filter.

The TurPol data were obtained using the UBV mode of the polarimeter with high voltage for the R and I photomultipliers switched off. The effective wavelengths of the UBV bands are 3600, 4400, and 5300 Å, respectively. With this mode, typical count rates of 10^6 counts s^{-1} were achieved giving a precision of 0.01% for a 3σ detection. Observations of two zero-polarization standards were acquired each night at the same precision in order to determine the instrumental polarization. The position angle calibration was obtained with observations of two high polarization standard stars. For interstellar polarizations, position angles do not depend significantly on the wavelength, allowing the use of weighted-averages from the UBV bands to achieve the highest possible precision; these 'broad-band' position angle measurements are listed in Table 2.

The early Tinbergen (1982) survey, made during 1973-1974 from La Silla (Chile) and Hartebeespoortdam (S. Africa) in the southern hemisphere, and Leiden (Netherlands) in the northern hemisphere, remains the most extensive all-sky survey of weak polarizations, with 1σ sensitivity on the Q and U Stokes parameters of 0.006–0.009 %, depending on the instrument and data set. These weak polarizations are biased towards larger polarization strengths, since $P^2 = Q^2 + U^2$ is always positive. Naghizadeh-Khouei & Clarke (1993b) evaluated the statistics of stars observed from each observing station in the Tinbergen data set, and concluded that residual instrumental polarizations may remain in the K-star data collected from Hartebeespoortdam. We have examined the data from Hartebeespoortdam for non-active K-stars that also have $P/dP> 2.5$. The seven stars that match the data criteria are located at angles of $86° \pm 32°$ from the ISMF direction defined by the center of the IBEX Ribbon arc. If the direction of the ISMF at the heliosphere is the same as in the local ISMF direction, then for a uniform ISM the maximum polarizations are expected at angles of $90°$ from the ISMF pole. We therefore assume that any contribution of instrumental polarization to the Hartebeespoortdam data is insignificant, while acknowledging that high-sensitivity observations and temporal monitoring of the polarizations of these stars are needed.

This study also includes the Bailey et al. (2010) polarizations of nearby stars obtained with the PlanetPol instrument at the William Herschel telescope. These linear polarization data were collected over a broad red band (maximum sensitivities at 7000–8000Å), and achieved typical accuracies of parts-per-million. PlanetPol data were also included in the Paper I analysis, but without screening for stellar activity. Twenty-six stars in the PlanetPol catalog that passed the selection criteria above were incorporated into our analysis of the local ISMF direction and are listed in Appendix B. Bailey et al. (2010) measured 18 northern hemisphere stars that were also observed by Tinbergen, and detected weak polarizations towards roughly half of the stars that were

unpolarized at the sensitivities of the Tinbergen data.[4] PlanetPol data showed that polarizations in the $\mathrm{RA} > 17^{\mathrm{H}}$ region increased with distance, and measured a weak interstellar polarization of 17.2 ± 1.0 ppm towards α Lyr (Vega, HD 172167), 8 parsecs away. Bailey et al. argue that the face-on debris disk around Vega is unlikely to contribute to the observed polarization signal since the instrument aperture is 5" and the radius of the central hole in the disk is $11" \pm 2"$. We show that the α Lyr polarization data have follow polarization trends of other nearby stars (§5.3) so those data are retained in this sample.

Santos et al. (2011) surveyed interstellar polarizations towards Loop I for stars out to distances of 500 parsecs, using the imaging polarimeter at LNA. Typical mean accuracies $1\sigma = 0.05\%$ were achieved in the V-band. Forty stars in the Santos et al. catalog passed the regional and activity selection criteria above and are listed in the Appendix B.

Polarizations of stars used in the determination of the local ISMF direction (within 40 parsecs) are plotted against the distance of the star in Figure 3. For comparison, the polarizations of more distant stars (40-110 parsecs) within $90°$ of the heliosphere nose are also shown (from the catalogs of Santos et al. 2011; Heiles 2000; Leroy 1993, 1999). A general increase in polarization strength with distance is seen (this is discussed in more detail in Appendix C). The polarizations shown in Figure 3 were measured in different bandpasses. For the PlanetPol bandpass covering red wavelengths (Bailey et al. 2010), the Serkowski curve of polarization versus $\lambda/\lambda_{\mathrm{max}}$ predicts polarizations that are up to 30% below the peak polarizations at λ_{max} (λ is the wavelength of observation and λ_{max}, which has a median value ~ 5500 Å, is the wavelength of maximum polarization, Serkowski et al. 1975). The PlanetPol stars, located in the northern galactic hemisphere, includes the largest set of detection of very weak polarizations, while the early Tinbergen (1982) dataset provide the most detections in the southern hemisphere. For this reason, polarization strengths are not used in Paper I to trace the ISMF direction. With the addition of new high-sensitivity data in the southern hemisphere, all polarization position angle data can be included in the study using weighted fits (§4.2).

Cool stars are included as target stars to provide adequate spatial coverage, but not all cool stars are suitable for the high-sensitivity interstellar polarizations of $\sim 0.01\%$ needed for this study. Magnetic activity is observed in cool stars, especially late K and M stars. With the sensitivity levels for most observations used in this study there is no *a priori* reason to omit stars with active chromospheres from the sample, however some cool stars are known to show polarizations in chromospheric lines (Clarke & Fullerton 1996). Stars of spectral types G and cooler, and with known active chromospheres, are usually omitted from the data sample used to evaluate the local

---

[4]Note that the data listed for several of the Tinbergen measurements in Table 2 of Bailey et al. (2010) contains typographical errors (Philip Lucas, private communication).

ISMF direction. Screening for active stars was performed using the lists in Gray et al. (2006). For the same reason, variable stars with variations $\delta V \geq 0.06$ mag are omitted to avoid other intrinsic magnetic phenomena, by requiring the coarse variability flag, VarFlag word H6, in the Hipparcos catalog (Perryman 1997)[5] to be H6=1. The analysis in Paper I did not screen for stars with known chromospheric activity.

4.   Results

4.1.   ISMF direction from unweighted fit

The first evaluation of the best-fit ISMF direction uses the same basic method as in Paper I, but applied to the larger set of data in this paper (§3). Equation 1 was evaluated for F_i with G_n=1, using data points where $P/dP >$ 2.5. All observations meeting the selection criteria (§3) are used in the fit, including measurements of the same star by different observers. The application of eqn. 1 to the polarization data set (§3) yields an ISMF direction toward ℓ,b=37° $\pm$ 15°, 22° $\pm$ 15° (see Table 1 for ecliptic coordinates). There is no significant change in the direction obtained from the unweighted fit when compared to the results of Paper I. The values of F_i are displayed in Figure 5, in both both ecliptic and galactic coordinates, and for each point in the possible ISMF grid using the 1° grid spacing discussed in §2.

Because of the underlying data sample, the unweighted fit emphasizes southern hemisphere data acquired in the 1970's. For the best-fit ISMF direction, $B_{i=best}$, 48 stars contributed to give $F_{i=best}$= 0.51 for the function being minimized. Of these 48 stars, 20% have new NOT and LNA data and they contributed 25% of $F_{i=best}$, 35% have pre-1980 data from Tinbergen (1982) or Piirola (1977) and they contributed 29% of $F_{i=best}$, 31% have PlanetPol data and they contributed 32% of $F_{i=best}$, and 8% were observed by Santos et al. (2010) and they contributed 12% of $F_{i=best}$. Note that no single set of observations appears to dominate this result.

4.2.   ISMF direction from weighted fit

The new high-precision polarization data in the southern hemisphere, as well as additional high-precision data in the northern hemisphere, (§3) makes it possible to evaluate the best-fit ISMF direction by utilizing all of the position angles in the sample, by weighting each value according by the position angle probability distribution in eqn. 2.

---

[5]See the VizieR catalog I/239/.

If the polarizing medium were to be homogeneous over the nearest 40 parsecs in the galactic hemisphere (which is not the case), combining polarization data using weighted values implicitly weights the resulting field direction towards more distant points where the signal-to-noise (S/N) is larger. If in contrast there is no statistically significant field in the same spatial region, the resulting field direction based on weighted fits is close to the center of the spatial interval for randomly distributed polarization directions.

For the weighted fits, the polarization strengths in the combined set of all data were capped at 50×10^{-5} in order to minimize the possible biases due to unrecognized intrinsic stellar polarization. Fewer than 5% of the significant ($P/dP > 2.5$) data points in the fit were affected by this cap. With the use of weighted fits, the best-fit direction is biased towards data sets that have low quoted uncertainties. To avoid over-reliance on the PlanetPol data, which are quoted to a typical accuracy of ppm and are spatially clustered in the northern hemisphere, the P/dP value input to G_n was capped at 3.5, and a lower limit of 10^{-5} was set on G_n. With these constraints, the best-fit ISMF direction is oriented towards $\lambda, \beta = 260^{+15}_{-20}$, 49 ± 15 or $\ell, b = 47° \pm 20°, 25° \pm 20°$ (Table 1). The values of F_i (eqn. 1) are plotted in Figure 6, using G_n given by eqn. 2. It is seen that the minimum value of F_i is more clearly defined for $G_n = 1$ than for G_n given in eqn. 2.

One hundred and seventy-seven stars have contributed to this best-fit ISMF direction, $B_{i=best}$. For this fit the mean value of eqn. 1 gives $F_{i=best} = 485$, using G_n from eqn. 2. Of these 177 stars, 26% have new NOT and LNA data and they contributed 11% of $F_{i=best}$; 39% have pre-1980 data from Tinbergen (1982) or Piirola (1977) and they contributed 24% of $F_{i=best}$; 12% have PlanetPol data and they contributed 60% of $F_{i=best}$; and 20% were observed by Santos et al. (2010) and contribute 0.3% of $F_{i=best}$. The PlanetPol contribution to the function being minimized, F_i, is dominated by four stars that have position angles nearly orthogonal (90^{+25}_{-15} degrees) to the meridians of $B_{i=best}$ and that make 86% of the PlanetPol contribution. Those four stars are HD 150680 at 10 parsecs, and three high-latitude stars at 24–31 parsecs (HD 113226, HD 116656, and HD 120315).

This method of using weighted fits produces an ISMF direction that is biased by the distribution of measurement errors for diverse instruments. We have tested the effect of the weighting factor by raising the lower limit of G_n to 10^{-4} for $P/dP \leq 3.5$. This test increases the homogeneity of low significance data points. Although the resulting ISMF direction is within 25° of $B_{i=best}$, it is closer to the center of the spatial interval indicating increased reliance on statistically insignificant measurements. The cap $P/dP \leq 3.5$ in G_n (eqn. 2) has the effect of deemphasizing the PlanetPol data where the ppm-level uncertainties otherwise dominate the result. If instead, we take $G > 10^{-5}$ and a P/dP cap of 4–6, the magnetic pole is then directed towards $\ell = 337° \pm 10°$ and $b = 28° \pm 7°$ and the F minimum (eqn. 1) becomes very poorly defined. We are quoting the best-fit ISMF direction for the weighted fit (Table 1) for values $P/dP \leq 3.5$ and $G_n \geq 10^{-5}$, since these limits

appear to present the best overall representation of the data given the differences in measurement sensitivities. With future high-sensitivity data, it should be possible to treat the analysis utilizing a broader range of the weighting factor.

5. Discussion

5.1. Comparing the ISMF directions traced by the IBEX Ribbon and polarizations

The very local ISMF direction provided by the center of the IBEX Ribbon arc is separated by 32^{+27}_{-30} degrees from the direction of the best-fit ISMF (weighted fit in Table 1). MHD heliosphere models that sucessfully predict the location of the IBEX Ribbon yield offsets between the center of the Ribbon arc and the interstellar magnetic field that shapes the heliosphere of between $0°$ and $15°$ (Heerikhuisen & Pogorelov 2011), so the direction of the very local ISMF found here is marginally consistent with the direction of the ISMF that shapes the heliosphere. Polarization of stars within 40 pc and $90°$ of the heliosphere nose have contributed to this result. Up to fifteen interstellar clouds have been identified towards stars in this region of space (Lallement et al. 1986; Frisch et al. 2002; Frisch 2003; Redfield & Linsky 2008; Frisch et al. 2011). The magnetically aligned dust grains causing the polarizations presumably are located in these clouds. Although local color excess values are too small to be measured, the variable gas-phase abundances of the refractory elements that make up the grains show that several types of interstellar grains must be present in these clouds (Frisch & Slavin 2012). The clouds are distinguished by the gas kinematics using the assumption of solid-body motion, and in some cases by temperature. Since most of the neutral ISM that is within 40 parsecs is also within 20 parsecs (§3), the best-fit ISMF direction then may represent primarily the ISMF direction within ~ 20 parsecs of the Sun. This would help explain the remarkably similar directions of the ISMF traced by the IBEX Ribbon and the polarization data.

If the IBEX ENA Ribbon and interstellar polarizations trace the same ISMF direction, then polarization strengths should increase with ENA fluxes because interstellar polarizations and the IBEX Ribbon both reach maximum strengths in sightlines that are perpendicular to the magnetic field, e.g. where $B \cdot R$=0 for magnetic field B and radial sightline R. Figure 10 shows a plot of the mean value of 1.1 keV ENA fluxes that are in a $12°$ diameter region centered on stars that are within 40 parsecs, $90°$ of the heliosphere nose, and have $P/dP> 2.5$. ENA fluxes with signal-to-noise S/N> 3.5 are included. The data points are color-coded according to the data source in the left figure. Data in Figure 10, left, tend to be divided into four groups with different relations between the polarization and ENA fluxes. Group A consists of the highest quality data, such as data collected for this study and the PlanetPol data (§3), and show a general increase of polarization with

ENA fluxes. The PlanetPol stars in group A are located in the $\mathrm{RA} = 16^{\mathrm{H}} - 20^{\mathrm{H}}$ interval. Region D primarily represents 1970's polarization data, where uncertainties are substantially larger. The trend in region B is ambiguous. The four groups of data in Figure 10, left, are plotted in galactic coordinates in Figure 10, right using a color-coding that shows the data group. The increase of ENA fluxes with polarization for stars in group A supports the hypothesis that the ISMF sampled by the polarization data and Ribbon ENA fluxes are tracing the same, or similar, ISMF directions. Results for the remaining stars are ambiguous.

The difference between the ISMF directions from the polarization and ENA Ribbon data may reveal structural components of the local ISM. The polarization data set we use to determine the field direction (§3) may not sample the interstellar cloud surrounding the Sun, the LIC. The Sun is within 20,000 AU of the edge of the LIC (Frisch et al. 2011), and the LIC includes a minimal amount of ISM within 90° of the heliosphere nose (e.g. Redfield & Linsky 2008). It is possible that the ISMF direction traced by the center of the IBEX Ribbon arc represents the ISMF in the LIC, while the ISMF traced by the polarization data represents the ISMF traced by the next cloud in the upwind direction, the G-cloud that is observed towards the nearest star α Cen. The LIC is $\sim 22\%$ ionized (Slavin & Frisch 2008, Appendix A), and the G-cloud is likely to be partially ionized, so that the ISMF will couple tightly to the gas in these clouds. The possible location of the ISMF traced by polarization data is discussed further below where a small rotation with distance of the local ISMF is found (§5.3.2). This rotation suggests that some of the small difference between the ISMF directions found from the IBEX Ribbon and polarization data may result from the volume-averaged ISMF direction implicit in our method for fitting the polarization data.

5.2. Local ISMF and Loop I

The relation between the Loop I superbubble and the ISM within 20 pc has been known for some time (see review of Frisch et al. 2011). Recently, Wolleben (2007) modeled the polarized low-frequency 1.4 GHz and 23 GHz radio continuum of Loop I, including the North Polar Spur emission, as arising from two spherical shells, denoted "S1" and "S2", each with a swept up magnetic field traced by polarized synchrotron emission.[6] An ordered magnetic field structure is implicit to the Wolleben model. His shell parameters suggest that the Sun is in the rim of the S1 shell, which is centered 78 ± 10 parsecs away towards $\ell = 346° \pm 5°, b = 3° \pm 5°$. Previous studies reached similar conclusions, although with a single superbubble so that the center of the H° shell is $\sim 12°$ south of the center of the radio continuum shell (e.g. Heiles 1998a). The direction of the

---

[6]Loop I is sometimes referred to as the 'North Polar Spur', which historically is the brightest part of the radio continuum loop and juts vertically from the galactic plane near longitudes of $\sim 30°$ (e.g., Hanbury Brown et al. 1960).

swept-up ISMF in the S1 shell (which has generous uncertainties) is consistent with the magnetic field direction in the local polarization patch found by Tinbergen (1982); any local fragments of the S1 and S2 shells are not spherical, however, since the Fe^+ column densities in local ISM do not trace these features defined by Wolleben (Frisch 2010). The Wolleben model provides a convenient quantitative relation between the large-scale ISMF defined by Loop I and the ISMF close to the Sun.

Local cloud kinematics, the local ISMF, and local gas-phase abundances all suggest an origin related to Loop I. In the local standard of rest (LSR), the local cluster of clouds flows past the Sun at a bulk velocity of $V = -17\,\mathrm{km\,s^{-1}}$, and towards us from the direction $\ell,b \sim 335°, -5°$ (Frisch et al. 2011). Solid-body motion is assumed in determining this vector. The flow direction is $\sim 14°$ from the center of the S1 shell, which is located at $\ell,b \sim 335°, -5°$. Although the S1 shell is an evolved superbubble remnant, the local fragment of the shell appears to still be radially expanding into the low density region of the Local Bubble. The best ISMF direction from the weighted fit (Table 1) makes an angle of $76°$ with the local ISM bulk flow vector. These numbers are consistent with a scenario where the normal to the shell rim is parallel to the ISM velocity, and the magnetic field is compressed in the shell rim so that the field direction is nearly perpendicular to the normal of the shell surface. An association of local ISM with a supernova shell is consistent with the high and variable abundances of the refractory elements Fe, Mg, and Si in local ISM, which suggest inhomogeneous grain destruction by interstellar shocks (Frisch et al. 2011; Frisch & Slavin 2012).

5.3. Ordered ISMF near Sun

A detailed study of the behavior of interstellar polarizations and ISMF behavior with distance is possible with the sensitive PlanetPol data for stars located in the interval $\mathrm{RA} = 16^{\mathrm{H}} - 20^{\mathrm{H}}$, which contains the $\mathrm{RA} > 17^{\mathrm{H}}$ region where Bailey et al. (2010) found an increase of polarization with distance. This region overlaps the low latitude part of the North Polar Spur, where aligned optical polarization vectors define the ISMF for distances 60–120 parsecs (Mathewson & Ford 1970; Santos et al. 2011). The behavior of the ISMF for distances < 60 parsecs in the North Polar Spur direction is provided by PlanetPol data.

5.3.1. Polarization versus distance and column density in $16^{\mathrm{H}} - 20^{\mathrm{H}}$ region

Bailey et al. (2010) found that the increase of polarization with distance was greater for stars with $\mathrm{RA} > 17^{\mathrm{H}}$ than for stars in other spatial intervals. The increase of polarization with star distance for PlanetPol stars in the $\mathrm{RA} = 16^{\mathrm{H}} - 20^{\mathrm{H}}$ region and with $P/dP > 3.0$ is shown in

Figure 7, right. For this set of uniform quality data a maximum value for the polarization is found for each distance interval within ~ 60 pc, and there are no observed points that lie above the upper envelope marked by the filled points. Polarizations of stars beyond that follow this trend. Stars which define this maximum are often refereed to as the polarization 'upper envelope' (e.g. Andersson 2012, also see Appendix C), and we use that term here. In general, polarization data tend to have an upper envelope when plotted against either distance or color excess due to either depolarization or patchy ISM. A rough estimate of the dependence of polarization on distance can be found by first binning stars into 10 parsec intervals, and then selecting the stars with the maximum polarization in each interval. Omitting bins with no stars, seven stars (filled circles in Figure 7) can be used to define the upper limit of polarization as a function of distance. A linear fit though the envelope stars gives the approximate distance dependence of the maximum polarization in the $\mathrm{RA} = 16^{\mathrm{H}} - 20^{\mathrm{H}}$ region of

$$\log P \sim 1.200 + 0.013 * D \tag{3}$$

where P is polarization in ppm and D is the distance in parsecs. The closest envelope star is α Lyr at 8 parsecs (Table 3 lists the envelope stars). The locations of the $\mathrm{RA} = 16^{\mathrm{H}} - 20^{\mathrm{H}}$ stars are plotted in galactic coordinates in Figure 7, left. Two unpolarized PlanetPol stars in this region are not plotted, HD 163588 and HD 188119, both of which are located at larger longitudes than the other stars. Stars that form the upper envelope of the polarization-distance relation are loosely confined between galactic longitudes of $30°$ and $80°$, and latitudes of $–5°$ to $30°$.

The upper envelope of the polarization-distance relation (Figure 7) can be used to estimate the gas density gradient along the ISM holding the ISMF, since dust and gas have similar spatial distributions in diffuse clouds. Few of the PlanetPol stars have measured $\mathrm{H^o}$ or $\mathrm{D^o}$ column densities (e.g. Wood et al. 2005), so column densities are estimated by converting polarization to color excess, and then converting color excess to $N(\mathrm{H})$, using standard relations for diffuse clouds. The polarization for dust grains aligned by an ordered ISMF, with no random component, provides an upper envelope of the P vs. $E(\mathrm{B–V})$ relation of $P(\%) = 9E(B - V)$ (Fosalba et al. 2002). Interstellar gas and dust have similar spatial distributions in the low opacity ISM. *Copernicus* observations of the saturated $\mathrm{H^o}$ $\mathrm{Ly}\alpha$ absorption line and molecular hydrogen lines showed that $N(\mathrm{H})/E(\mathrm{B–V})=N(\mathrm{H^o}+ \mathrm{H_2})/E(\mathrm{B–V})= 5.8 \times 10^{21} \cdot$ cm^{-2} mag^{-1} (Bohlin et al. 1978).[7] The *Copernicus* value underestimates hydrogen column densities for partially ionized gas since independent measurements of ionized gas are not available for most sightlines. The relation between polarization and column density is estimated by combining the distance-polarization fit with the empirical P vs.

---

[7]We use the ratio for the ISM towards all stars, rather than the ratio for the intercloud medium, $N(\mathrm{H^o}+ \mathrm{H_2})= 5.0 \times 10^{21} \cdot E(\mathrm{B–V})$ cm^{-2}, that might be relevant to the nearest ISM (Bohlin et al. 1978).

E(B–V) and E(B–V) vs. N(H) relations, giving

$$\log N(\mathrm{H}) = 18.01 + 0.013 * D. \tag{4}$$

for stars tracing the upper envelope of the P-E(B–V) relation and P-distance relation. For other stars, foreground depolarization can lead to lower values for N(H°). This gas-distance relation can be checked against three nearby stars in the RA $= 16^{\mathrm{H}} - 20^{\mathrm{H}}$ region with N(H°) values determined by Wood et al. (2005), HD 155886 (36 Oph), 165341 (70 Oph), and HD 165185. The ratio of the predicted N(H) (eqn. 4) to the observed N(H°) for these three stars is 1.35 ± 0.35, indicating depolarization and/or inhomogeneous ISM is present nearby.

5.3.2. *Polarization versus position angle in* $16^{\mathrm{H}} - 20^{\mathrm{H}}$ *region*

Optical polarization data that traces the H° filamentary structure of Loop I beyond ~ 80 parsecs reveal an ordered ISMF that follows the axis of an H I filament of Loop I (Heiles 1998a). Optical polarization vectors (Figure 4), and the location of the RA $= 16^{\mathrm{H}} - 20^{\mathrm{H}}$ region towards the North Polar Spur, suggest that the very local ISMF direction may also be ordered. Figure 8 displays the polarization position angles, PA$_{\mathrm{RA}}$, for PlanetPol stars with $P/dP > 3.0$ in this interval, as a function of distance. With the exception of the outlier star HD 164058, which has PA$_{\mathrm{RA}} = 145° \pm 0.5°$ and a distance of 45 parsecs, the envelope stars within 55 parsecs display a smooth rotation of polarization position angle with distance. HD 164058 is a K5III star and belongs to a spectral class where intrinsic polarization occurs because of chromospheric magnetic activity and was omitted from the fit in eqn. 5 as an obvious outlier (see below). A linear fit to position angles versus distance gives

$$PA_{\mathrm{RA}}(\mathrm{D}) = 35.97(\pm 1.4) - 0.25(\pm 0.03) \cdot \mathrm{D} \tag{5}$$

and a χ^2 of 0.559, where PA_{RA} is in degrees and the distance D is in parsecs. The small value of χ^2 per degree of freedom (2) suggests that the uncertainties on PA$_{\mathrm{RA}}$ quoted by Bailey et al. (2010) may be generous. [8] The probability that the computed χ^2 value would have a value larger than 0.559 is 0.76, indicating that parameters of the fit in eqn. 5 are believable. After excluding HD 164058, the relation between the polarization direction and star distances of the four envelope stars within 55 parsecs appears to be linear. The large difference of $7.8\sigma_{\mathrm{pp}}$ between the position angle of the outlier star and the best-fit line (eqn. 5), where σ_{pp} is the mean difference between the best-fit

---

[8]Bailey et al. (2010) include several different effects when calculating uncertainties for their measurements, including counting statistics, possible intrinsic telescope polarization, and in some cases atmospheric polarization caused by Sahara dust.

line and the position angles of PlanetPol stars within 55 pc except for the outlier, justifies omitting HD 164058 from the calcuation of eqn. 5. The envelope stars are partly self-selected by the fact they represent sightlines where intervening depolarization is minimized, so the linear fit to the polarization position angles suggests the existence of a nearby ordered ISMF that rotates $\sim 0.25°$ per parsec. This rotation is confined to the small region of space (filled dots in Figure 7, left) where Bailey et al. (2010) found the systematic increase in polarization strengths with distance (Figure 7, right). The envelope stars appear to sample the uniform part of an extended medium that contains a magnetic field and reaches to within 8 pc of the Sun.

The standard deviation of position angles around the ordered component is a measure of the magnetic turbulence in this region. For all stars in the $RA = 16^H - 20^H$ region and within 55 parsecs, excluding the outlier star, the standard deviation of polarization position angles about the best-fit line is $23°$, which we interpret as magnetic turbulence.

The smooth variation of the ISMF direction over distance suggests that the four nearest envelope stars are embedded in the polarizing medium, which extends between α Lyr (Vega, 8 parsecs) and δ Cyg (52 parsecs). The sightlines to all of the envelope stars sample either the S1 shell, the S2 shell, or both shells, according to the Wolleben (2007) model and the shell configurations plotted in Frisch (2010). The angular spread on the sky of the envelope stars is $50°$, which suggests that the ISMF in the nominal S1 and S2 shells consists of a homogeneous "matrix" component of smooth material that is sampled by the envelope stars, and patchy material and/or a turbulent ISMF that produces depolarization of, and turbulence in, the position angles of non-envelope stars.

If the polarizations of the envelope stars are tracing matrix ISM in this region, this material should be detectable as interstellar absorption features. Absorption lines have been measured towards the four envelope stars in the fit. All four stars show absorption at or close to the velocity of the Apex Cloud defined by Frisch (2003),[9] so it is tempting to assume that the 'Apex cloud' represents the smooth ISM filling the local region of the S1 and S2 shells. Interstellar absorption lines have also been measured towards a fifth polarized star, HD 187642, in region $RA = 16^H - 20^H$, where a component at the Apex cloud velocity is also found. Towards the envelope star HD 159561, the Apex cloud component is characterized by weak Ca^+ absorption and a typical ratio $Ti^+/Ca^+=0.41$, suggesting it contains some neutral gas since Ti^+ and H^o have the same ionization potential (Welty & Crowther 2010). A more recent and complete cloud identification scheme was developed by Redfield & Linsky (2008), where three of the Apex cloud components towards envelope stars are instead assigned to the MIC cloud, while the fourth component is left as unassigned. Three of the four stars in Redfield & Linsky (2004b) that are in the $RA = 16^H - 20^H$ region have components at the Apex velocity, however the cloud temperature

---

[9]This cloud vector is similar to the "Panoramix" cloud that was identified much earlier by Lallement et al. (1986).

ranges from $\sim 1,700 - 12,500$ K for these components. A second possible carrier of the ordered field is the 'G' cloud since it has a wide angular extent in the upwind direction, is within 1.3 parsecs of the Sun, and is observed towards the envelope stars. The identification of the cloud carrying the ordered component of the ISMF requires additional study.

5.3.3.   *Polarization versus interstellar radiation field in $16^{\mathrm{H}} - 20^{\mathrm{H}}$ region*

Radiative torques are known to play a role in the alignment of dust grains in dense clouds where the radiation field has a preferred direction (e.g. Andersson & Potter 2006; Draine & Weingartner 1997; Andersson et al. 2011; Lazarian & Hoang 2008), but this does not appear to be the case locally. The interstellar radiation field extrapolated to the location of each star in the $\mathrm{RA} = 16^{\mathrm{H}} - 20^{\mathrm{H}}$ region appears to anticorrelate with polarization strengths. We believe that this correlation is a chance coincidence of the relative locations of the brightest radiation sources and polarized stars. Figure 9 shows polarizations for stars inside (filled symbols) and outside (open symbols) of the $\mathrm{RA} = 16^{\mathrm{H}} - 20^{\mathrm{H}}$ region, plotted against the total far-UV 975Å flux that has been extrapolated to the position of each polarized star, while ignoring any possible opacity effects. The 975Å radiation flux is given by the 25 brightest stars at this wavelength (Opal & Weller 1984), which are primarily located in the third and fourth galactic quadrants because of the geometry and low opacity of the Local Bubble (see, e.g., the interstellar radiation field at the Sun from the S2 UV survey, Gondhalekar et al. 1980). These polarization data show a trend for linear polarization to increase as radiation flux decreases. The rough anticorrelation between radiation fluxes and polarizations is shown by the fit log $P = 4.61 - 0.054*F_3$ (dashed line in Figure 9), where P is in units of 10^{-6} and F_3 is the radiation flux at 975 Å in units of 10^3 photons cm^{-2} s^{-1} Å^{-1}. This apparent anticorrelation appears to be the result of the relative locations of the brightest hot UV-bright stars and the most distant polarized stars, that define the low-flux region of the trend (see Appendix D for more details).

5.3.4.   *CMB dipole anisotropy and the local ISMF*

Large scale global deviations from a uniform blackbody spectrum of the CMB radiation define a dipole anisotropy that is oriented towards $\ell = 263.85°\pm0.1°$ and $b = 48.25°\pm0.04°$ (Bennett et al. 2003). The great circle on the sky that is midway between the two poles of the CMB dipole displays a striking symmetry around the direction of the heliosphere nose direction defined by the flow of interstellar He$^\circ$ through the heliosphere (Frisch 2007). The best direction of the heliosphere nose is defined by the new IBEX consensus direction for the interstellar He$^\circ$ flow, which includes correction for propagation and ionization effects (McComas et al. 2012, see Appendix A). This

new consensus IBEX direction for the heliosphere nose more closely aligns the nose direction with the great circle that is midway between the hot and cold poles of the CMB dipole moment. The angle between the heliosphere nose and dipole anisotropy direction is $91.5° \pm 0.6°$. The probability that the great circle that is evenly spaced between the poles of the CMB dipole anisotropy, which is defined to within $\sim \pm 0.10°$, would pass through the $\sim 3° \times 3°$ area on the sky that includes the heliosphere nose direction, is less than 1/200. Figure 11 shows the great circle in the sky that is equidistant from the antipodes of the CMB dipole moment (gray line), as well as the hot (red) and cold (blue) dipole directions.

The 90-degree great circle midway between the dipole directions also passes through the best-fit ISMF direction, when uncertainties are included (Table 1). The ISMF direction from the weighted fit us plotted as a purple dot in Figure 11, together with the uncertainties on this direction (purple polygon) and the 90-degree circle. That the great-circle dividing the antipodes of the CMB dipole moment would also pass through the ISMF pole, which is defined by an area of ~ 300 square-degrees, including uncertainties, is less than one in 10^4. A deeper knowledge of the configuration and properties of the global heliosphere and local ISMF will elucidate whether additional CMB foregrounds might be present.

Although a possible relation between the CMB dipole and heliosphere may seem far-fetched, a number of studies have shown that the symmetries traced by the low-ℓ CMB moments are not consistent with the predictions of gaussianity of the universe based on standard cosmological models, and in particular the quadrupole and octopole moments show evidence of the ecliptic geometry (e.g. Schwarz et al. 2004; Starkman et al. 2009, and citations in and to these articles). Since the ISM flows through the heliosphere from a direction $5°$ above the ecliptic plane, these low-ℓ symmetries are equivalent to symmetries around the heliosphere nose (e.g. see Figures 6 and 7 in Frisch 2007). Unrecognized CMB foregrounds related to the heliosphere may be present, with the most likely candidate being emission from interstellar dust inside the heliosphere since the dust traces both the gas flow and ISMF direction (Slavin et al. 2012; Frisch & Slavin 2012; Slavin et al. 2009).

5.4. Speculative implications

5.4.1. Local ISMF: Interarm or Arm?

Comparisons between the ISMF at the heliosphere and the ISMF observed in other nearby regions provides insight into the uniform and random components of the local ISMF, such as whether the field has the large-scale coherence of interarm fields or of the small-scale random fields seen in spiral arm regions. Random components of the ISMF in spiral arms are coherent over

scale sizes of 5–50 parsecs; Faraday rotation structure functions indicates a more turbulent ISMF with outer scales of 10–20 parsecs (Rand & Kulkarni 1989; Haverkorn et al. 2006). In contrast, Faraday rotation measures for interarm sightlines show a more uniform component that is coherent over scales of 100-200 parsecs. The ratio of the uniform to random components of interstellar polarizations in the plane of the sky is typically ~ 0.8, when global polarization data are considered (Fosalba et al. 2002).

If the local ISMF sampled by the IBEX Ribbon and optical polarization data is part of an ISMF that is coherent over several hundred parsecs, the coherence should appear in the ISMF direction obtained from Faraday rotation measure (RM) data on nearby pulsars that yield an electron-density weighted measurement of the parallel component of the ISMF. Salvati (2010) fit the RM and dispersion measures of four nearby (distances 160–290 parsecs) pulsars that sample the low density interior of the Local Bubble in the third galactic quadrant ($\ell \sim 180° - 270°$). The ISMF strength obtained from these data is 3.3 μG, and the field is directed towards $\ell, b \sim 5°, 42°$. The third galactic quadrant is opposite to the $\mathrm{RA} = 16^\mathrm{H} - 20^\mathrm{H}$ region in the sky. The difference in the direction of the ISMF traced by the RM data and IBEX Ribbon, $\sim 23°$, is easily accommodated by the field curvature indicated by the envelope stars in the $\mathrm{RA} = 16^\mathrm{H} - 20^\mathrm{H}$ region (including α Lyr 8 parsecs away), and may indicate that the ISMF around the Sun extends into the third galactic quadrant.

The strength of the ISMF that shapes the heliosphere, ~ 3 μG, is close to the field strength found from the pulsar data. At the heliosphere, magnetic field strength is estimated from the pressure equilibrium between the inner heliosheath ions traced by ENAs and the ISM, and from the magnetic tension required to produce the 44° offset between the observed ENA minimum and downwind gas flow direction (Schwadron et al. 2011), while in the LIC it is found from equilibrium between gas and magnetic pressures (Slavin & Frisch 2008). The polarity of the ISMF found from the pulsar RM data is directed towards $\lambda, \beta = 232°, 18°$, and therefore is directed upwards through the ecliptic plane (see Table 1 for galactic coordinates). Although the field direction is consistent with the local ISMF shaping the heliosphere, the polarity appears to be the opposite of the polarity built into most MHD heliosphere models (Appendix A).

In the opposite direction of the sky from the pulsars, the $\mathrm{RA} = 16^\mathrm{H} - 20^\mathrm{H}$ region tests the coherence of the ISMF along the sightlines that are tangent to the Loop I shell. The slow rotation of the nearby ordered field component and its extension to within 8 parsecs pf the Sun, together with the similarity of ISMF directions from the IBEX Ribbon and pulsar data, suggests that the Loop I ISMF may extend into the third galactic quadrant. Figure 1 shows that the dust cavity caused by the Loop I expansion covers the northern polar cap and extends into the third galactic quadrant at high latitudes. The coherence of the ISMF can be found by comparing values from these three regions: (1) at the solar location, from the center of the IBEX Ribbon arc (to within $\sim 15°$, see Appendix A); (2) the nearest 40 parsecs in the galactic center region, including the tangential direction of

Loop I where the ordered component of the ISMF is found; (3) the low density void of the Local Bubble in the third galactic quadrant. The Sun is located (by definition) in region 1, and between regions 2 and 3. The difference in the ISMF directions determined from regions 1 and 2 is $\sim 32°$, and it is $\sim 22°$ between regions 1 and 3. The field curvature must extend from region 2, through the solar location in region 1, and into the third galactic quadrant corresponding to region 3. These data suggest that the local ISMF at the heliosphere is part of a large scale field that extends several hundred parsecs in space, such as is characteristics of interarm regions. The Loop I ISMF may be "opening out" into an interarm field as it expands into the low density third galactic quadrant.

5.4.2. *Galactic cosmic rays and the local ISMF*

Galactic cosmic rays (CR) in the energy range of 50 GeV – 40 TeV trace the local ISMF because the gyroradius is on the order of several hundred AU in a 1 μG magnetic field. Large scale anisotropies and smaller scale excess regions, have been detected in the distribution of CRs in this energy range (Nagashima et al. 1998; Hall et al. 1999; Abdo et al. 2008; Abbasi et al. 2011; Surdo & Argo-Ybj Collaboration 2011). It has been suggested that the Sun is located in a magnetic flux tube in the ISM, and that such a flux tube would be a conduit for galactic cosmic rays (GCRs) (Frisch 1997). Cox & Helenius (2003) presented a model of the Local Bubble that placed the Sun in a flux tube that has detached from the walls of the Local Bubble. Schwadron et al. (2012) have identified anisotropies in the CR distribution towards the heliotail direction caused by the propagation of CR's through the magnetic structure surrounding the heliosphere. Therefore it is an interesting exercise to compare the GCR asymmetries with the local ISMF direction.

Using cosmic ray fluxes in the northern and southern hemispheres, Nagashima et al. (1998) described two anisotropies in terms of a broad sidereal galactic anisotropy, and a narrow anisotropy, the "tail-in" anisotropy, described by a maximum towards the anti-apex direction of the solar motion.[10] The galactic anisotropy arrives from the direction $\alpha, \delta = 0^H, -20°$ ($\ell, b \sim 61°, -76°$). The tail-in excess corresponds to the direction $\alpha, \delta = 6^H, -24°$ ($\ell, b \sim 230°, -21°$), with a half-width of $\sim 68°$ and a maximum effect near $\sim 10^3$ GeV. The tail-in excess was originally attributed to the heliotail because it is approximately opposite to the direction of the solar motion through the LSR. Hall et al. (1999) fit the anisotropies as Gaussian features, and found a direction of maximum anisotropy for the tail-in excess towards $\alpha, \delta \sim 4.6^H, -14°$ ($\ell, b \sim 210°, -36°$), and a loss-cone centered at $\alpha, \delta \sim 13^H, 0°$ ($\ell, b \sim 123.°, 63.°$). To within the uncertainties, the direction of the

---

[10]The solar apex motion corresponds to a velocity of 18 ± 0.9 km s^{-1} directed towards $\ell \sim 47.9° \pm 3.0°, b = 23.8° \pm 2.0°$, however these values changes on a fairly regular basis with improved understanding of the astrometric data for the comparison stars used to establish the solar motion.

tail-in excess found by Hall et al. overlaps both the downwind He$^\mathrm{o}$ flow vector that defines the tail of neutral ISM gas behind the heliosphere, and the axis of the ISMF direction determined from the weighted fit (towards $\ell,b= 229° \pm 30°, -28° \pm 30°$). Figure 11 shows the directions of the ISMF, tail-in excess compared to the ISMF direction, and the true heliotail corresponding to the ENA flux minimum centered $\sim 44°$ west of the downwind gas flow (Schwadron et al. 2011).

6. Summary and conclusions

We have determined the direction of the interstellar magnetic field within 40 parsecs of the Sun and 90° of the heliosphere nose ($\sim 15°$ from the galactic center) using starlight polarized by magnetically aligned interstellar dust grains. The analysis is based on the assumption that the polarization E-vector is parallel to the direction of the ISMF and builds on the analysis in Paper I (Frisch et al. 2010a). The new technique for finding the ISMF direction minimizes the mean of an ensemble of sines of polarization position angles (§2). The use of an expanded data set, including new polarization data that have been acquired at several observatories for this study (§3), permits the use of weighted fits to the ISMF (§4) as opposed to the unweighted fit used in Paper I. The best-fit ISMF from the weighted fit is towards $\ell,b= 47° \pm 20°, 25° \pm 20°$. The direction obtained from the unweighted fit is consistent with the results of the weighted fit (Table 1).

The best-fit ISMF directions obtained from the weighted fit and from the center of the IBEX Ribbon arc (Table 1) are separated by 32^{+27}_{-30} degrees (§5.1). Although heliosphere models indicate that there could be a small offset between the direction of the ISMF shaping the heliosphere and the Ribbon arc center ($0 - 15°$), the agreement between these two field directions is remarkable considering that the polarization-based measurement is determined from light of stars up to 40 pc away. The similarity of these directions encourages the conclusion that the nearby ISMF is coherent over decades of parsecs, while the difference indicates that the local ISMF either has a curvature or is turbulent.

Interstellar optical polarizations reach maximum strengths in directions perpendicular to the ISMF, and the IBEX Ribbon appears in directions perpendicular to the ISMF draping over the heliosphere. Hence if the directions of the best-fit ISMF and magnetic field traced by the IBEX Ribbon are related, the polarization strengths and ENA fluxes will be proportional. In one region of the sky that touches the Ribbon, where the ISMF is observed within 8 pc of the Sun, ENA fluxes and polarization strengths are found to increase together (§5.1). This effect is seen only in the most sensitive polarization data.

In one region of the sky in the right-ascension interval $\mathrm{RA} = 16^\mathrm{H} - 20^\mathrm{H}$, Bailey et al. (2010) used their high-sensitivity PlanetPol data to conclude that polarization systematically increases

with distance (§5.3.1). Using stars that form the upper envelope of the polarization versus distance relation in that region, we find that $\log P = 1.200 + 0.013 * D$. For standard relations between polarization and color excess, and color excess versus $N(\text{H})$, the distant-dependent increase in column density in this spatial interval becomes log $N(\text{H})$=18.01+0.013*D; the relation overpredicts the actual $N(\text{H}°)$ measured for several stars by $\sim 35\%$.

This same region, which overlaps a low-latitude portion of Loop I, appears to contain an ordered ISMF that extends to within 8 parsecs of the Sun (§5.3.2). Stars forming the upper envelope of the polarization-distance relation define a unique group where foreground depolarization is minimized. For the nearby envelope stars, the polarization angle depends on the star distance with the relation $\text{PA}_{\text{RA}}= 35.97(\pm 1.4) - 0.25(\pm 0.03) \cdot \text{D}$ (§5.3). The ISMF rotates by $\sim 0.25°$ pc^{-1}, yielding a $10°$ ISMF rotation over a 40 parsecs thick magnetic layer. The nearest polarized star showing the ordered ISMF is HD 172167 (α Lyr, 8 parsecs), where the polarization direction is consistent with the direction of best-fit ISMF field. The dispersion of position angles about this nearby ordered ISMF component suggests that the turbulent ISMF component is $\sim \pm 23°$. These results are conditioned on the exclusion of a 7.8σ outlier star from the analysis, and on the small number of stars (4) available for defining the position angle rotation. Confirmation of this result would require observations at ppm accuracy towards very faint stars, V> 6 mag, in the spatial interval $\ell \sim 25° - 70°$, $b \sim 0° - 325°$.

The best-fit magnetic field direction, the flow of local ISM past the Sun, and variable abundances of refractory elements in the local ISM all suggest that the local ISM is associated with an expanding fragment of the S1 shell of the Loop I superbubble (§5.2). The bulk LSR flow of the local ISM past the Sun has an upwind direction within $15°$ of the center of the S1 shell. The best-fit ISMF makes an angle of $\approx 76°$ with the flow direction, suggesting the field is parallel to the rim and perpendicular to the flow velocity. Such a configuration would be expected for an ISMF swept up and compressed in an expanding superbubble shell. Variable abundances of refractory elements in local ISM indicate recent shock destruction of some of the local dust grains. A consistent interpretation of the kinematics of the local ISM and the direction of the best-fit ISMF would be that the ordered component represents the ISMF that was been swept up in the expanding S1 superbubble shell. The flow of ISM past the Sun is decelerating, as shown by the deviations of velocity components from a rigid-body flow (Frisch et al. 2011). Cloud collisions in the decelerating flow may generate the observed magnetic turbulence of $\pm 23°$, with the ordered component representing the matrix ISM between the clouds.

Polarization strengths for the envelope stars in region $\text{RA} = 16^{\text{H}} - 20^{\text{H}}$ anticorrelate with the interstellar radiation field at 975Å (§5.3.3). This anticorrelation is probably due to the fact that those stars are in the first galactic quadrant and, by chance, the most distant of those stars are also the most distant from the bright stellar far ultraviolet and extreme ultraviolet radiation sources that

are mainly located in the third galactic quadrant.

The ISMF direction from pulsars in the third galactic quadrant is within $22°$ of the ISMF direction from the IBEX Ribbon. A common field strength of $\sim 3\ \mu$G is found from the pulsar data, a range of heliosphere diagnostics including plasma pressure and the deflection of the heliotail, and models of the ionization of the ISM surrounding the heliosphere. This suggests that the ISMF near the Sun is coherent over large spatial scales, such as expected for interarm regions. One source of uncertainty is the polarity of the field, since the polarity derived from pulsar data is opposite in direction from the polarity that is assumed by several of the MHD heliosphere models.

The new ISMF direction, together with the new consensus direction for the ISM flow through the heliosphere derived from IBEX observations of interstellar He^o, strengthens the spatial coincidence between the geometry of the CMB dipole moment, the heliosphere nose, and the local ISMF (§5.3.4). The great circle that divides the two poles of the CMB dipole moment passes within $1.5° \pm 0.6°$ of the heliosphere nose defined by the IBEX measurements of the flow of interstellar He^o in the heliosphere, and passes through the best-fit ISMF determined by weighted fits to polarization position angles, to within the uncertainties.

The axis of the best-fit ISMF direction from polarization data extends through the direction of the 'tail-in' excess of GeV–TeV cosmic rays that has been attributed to the heliotail. The direction of the tail-in excess coincides poorly with the flow of interstellar He^o through the heliosphere.

High-sensitivity interstellar polarization data provide an opportunity to explore the ISMF and magnetic turbulence in the very diffuse ISM close to the Sun, and our very local galactic environment. The implications of understanding this field may affect our understanding of the most distant reaches of the Universe. The domain of the heliosphere and the local ISM are filters through which all observations about our more distant universe must pass.

REFERENCES

Abbasi, R., Abdou, Y., Abu-Zayyad, T., Adams, J., Aguilar, J. A., Ahlers, M., Altmann, D.,

Andeen, K., Auffenberg, J., Bai, X., & et al. 2011, ApJ, 740, 16

Abdo, A. A., Allen, B., Aune, T., Berley, D., Blaufuss, E., Casanova, S., Chen, C., Dingus, B. L., Ellsworth, R. W., Fleysher, L., Fleysher, R., Gonzalez, M. M., Goodman, J. A., Hoffman, C. M., Hüntemeyer, P. H., Kolterman, B. E., Lansdell, C. P., Linnemann, J. T., McEnery, J. E., Mincer, A. I., Nemethy, P., Noyes, D., Pretz, J., Ryan, J. M., Parkinson, P. M. S., Shoup, A., Sinnis, G., Smith, A. J., Sullivan, G. W., Vasileiou, V., Walker, G. P., Williams, D. A., & Yodh, G. B. 2008, Physical Review Letters, 101, 221101

Adams, T. F. & Frisch, P. C. 1977, ApJ, 212, 300

Andersson, B.-G. 2012, ArXiv e-prints/astro-ph:1208.4393

Andersson, B.-G., Pintado, O., Potter, S. B., Straižys, V., & Charcos-Llorens, M. 2011, A&A, 534, A19

Andersson, B.-G. & Potter, S. B. 2006, ApJ, 640, L51

Bailey, J., Lucas, P. W., & Hough, J. H. 2010, MNRAS, 405, 2570

Bennett, C. L., Halpern, M., Hinshaw, G., Jarosik, N., Kogut, A., Limon, M., Meyer, S. S., Page, L., Spergel, D. N., Tucker, G. S., Wollack, E., Wright, E. L., Barnes, C., Greason, M. R., Hill, R. S., Komatsu, E., Nolta, M. R., Odegard, N., Peiris, H. V., Verde, L., & Weiland, J. L. 2003, ApJS, 148, 1

Berdyugin, A., Piirola, V., & Teerikorpi, P. 2011, in Astronomical Society of the Pacific Conference Series, Vol. 449, Astronomical Society of the Pacific Conference Series, ed. P. Bastien, 157

Berkhuijsen, E. M. 1973, A&A, 24, 143

Bochsler, P., Petersen, L., Möbius, E., Schwadron, N. A., Wurz, P., Scheer, J. A., Fuselier, S. A., McComas, D. J., Bzowski, M., & Frisch, P. C. 2012, ApJS, 198, 13

Bohlin, R. C., Savage, B. D., & Drake, J. F. 1978, ApJ, 224, 132

Butters, O. W., Katajainen, S., Norton, A. J., Lehto, H. J., & Piirola, V. 2009, A&A, 496, 891

Chalov, S. V., Alexashov, D. B., McComas, D., Izmodenov, V. V., Malama, Y. G., & Schwadron, N. 2010, ApJ, 716, L99

Clarke, D. & Fullerton, S. R. 1996, A&A, 310, 331

Cox, A. N. 2000, Allen's Astrophysical Quantities (AIP Press), 29–30

Cox, D. P. & Helenius, L. 2003, ApJ, 583, 205

Davis, L. 1955, Physical Review, 100, 1440

Davis, L. J. & Greenstein, J. L. 1951, ApJ, 114, 206

de Geus, E. J. 1992, A&A, 262, 258

Draine, B. T. & Weingartner, J. C. 1997, ApJ, 480, 633

Florinski, V., Zank, G. P., Heerikhuisen, J., Hu, Q., & Khazanov, I. 2010, ApJ, 719, 1097

Fosalba, P., Lazarian, A., Prunet, S., & Tauber, J. A. 2002, ApJ, 564, 762

Frisch, P. C. 1990, in Physics of the Outer Heliosphere, ed. S. Grzedzielski & D. E. Page, 19–22

Frisch, P. C. 1995, Space Sci. Rev., 72, 499

—. 1996, Space Sci. Rev., 78, 213

Frisch, P. C. 1997

Frisch, P. C. 2003, ApJ, 593, 868

—. 2007, ArXiv e-prints:arXiv:0707.2970v2

—. 2010, ApJ, 714, 1679

Frisch, P. C., Andersson, B., Berdyugin, A., Funsten, H. O., Magalhaes, M., McComas, D. J., Piirola, V., Schwadron, N. A., Slavin, J. D., & Wiktorowicz, S. J. 2010a, ApJ, 724, 1473

Frisch, P. C., Dorschner, J. M., Geiss, J., Greenberg, J. M., Grün, E., Landgraf, M., Hoppe, P., Jones, A. P., Krätschmer, W., Linde, T. J., Morfill, G. E., Reach, W., Slavin, J. D., Svestka, J., Witt, A. N., & Zank, G. P. 1999, ApJ, 525, 492

Frisch, P. C., Grodnicki, L., & Welty, D. E. 2002, ApJ, 574, 834

Frisch, P. C., Heerikhuisen, J., Pogorelov, N. V., DeMajistre, B., Crew, G. B., Funsten, H. O., Janzen, P., McComas, D. J., Moebius, E., Mueller, H., Reisenfeld, D. B., Schwadron, N. A., Slavin, J. D., & Zank, G. P. 2010b, ApJ, 719, 1984

Frisch, P. C., Redfield, S., & Slavin, J. 2011, ARA&A, 49

Frisch, P. C. & Slavin, J. D. 2012, ArXiv e-prints/astro-ph:1205.4017

Funsten, H. O., Allegrini, F., Crew, G. B., DeMajistre, R., Frisch, P. C., Fuselier, S. A., Gruntman, M., Janzen, P., McComas, D. J., Möbius, E., Randol, B., Reisenfeld, D. B., Roelof, E. C., & Schwadron, N. A. 2009, Science, 326, 964

Gamayunov, K., Zhang, M., & Rassoul, H. 2010, ApJ, 725, 2251

Gondhalekar, P. M., Phillips, A. P., & Wilson, R. 1980, A&A, 85, 272

Gray, R. O., Corbally, C. J., Garrison, R. F., McFadden, M. T., Bubar, E. J., McGahee, C. E., O'Donoghue, A. A., & Knox, E. R. 2006, AJ, 132, 161

Grygorczuk, J., Ratkiewicz, R., Strumik, M., & Grzedzielski, S. 2011, ApJ, 727, L48+

Grzedzielski, S., Bzowski, M., Czechowski, A., Funsten, H. O., McComas, D. J., & Schwadron, N. A. 2010, ApJ, 715, L84

Hall, D. L., Munakata, K., Yasue, S., Mori, S., Kato, C., Koyama, M., Akahane, S., Fujii, Z., Fujimoto, K., Humble, J. E., Fenton, A. G., Fenton, K. B., & Duldig, M. L. 1999, J. Geophys. Res., 104, 6737

Hanbury Brown, R., Davies, R. D., & Hazard, C. 1960, The Observatory, 80, 191

Haverkorn, M., Gaensler, B. M., Brown, J. C., Bizunok, N. S., McClure-Griffiths, N. M., Dickey, J. M., & Green, A. J. 2006, ApJ, 637, L33

Heerikhuisen, J. & Pogorelov, N. V. 2011, ApJ, 738, 29

Heerikhuisen, J., Pogorelov, N. V., Zank, G. P., Crew, G. B., Frisch, P. C., Funsten, H. O., Janzen, P. H., McComas, D. J., Reisenfeld, D. B., & Schwadron, N. A. 2010, ApJ, 708, L126

Heiles, C. 1976, ARA&A, 14, 1

Heiles, C. 1998a, in Lecture Notes in Physics, Berlin Springer Verlag, Vol. 506, IAU Colloq. 166: The Local Bubble and Beyond, ed. D. Breitschwerdt, M. J. Freyberg, & J. Truemper, 229–238

—. 1998b, ApJ, 498, 689

—. 2000, AJ, 119, 923

—. 2001, ApJ, 551, L105

Heiles, C. 2009, in American Institute of Physics Conference Series, Vol. 1156, American Institute of Physics Conference Series, ed. R. K. Smith, S. L. Snowden, & K. D. Kuntz, 199–207

Jones, T. J., Klebe, D., & Dickey, J. M. 1992, ApJ, 389, 602

Kimura, H., Mann, I., & Jessberger, E. K. 2003, ApJ, 582, 846

Kurth, W. S. & Gurnett, D. A. 2003, J. Geophys. Res., 108, 2

Lallement, R., Quémerais, E., Koutroumpa, D., Bertaux, J., Ferron, S., Schmidt, W., & Lamy, P. 2010, Twelfth International Solar Wind Conference, 1216, 555

Lallement, R., Vidal-Madjar, A., & Ferlet, R. 1986, A&A, 168, 225

Lazarian, A. 2007, J. Quant. Spec. Radiat. Transf., 106, 225

Lazarian, A. & Hoang, T. 2008, ApJ, 676, L25

Leroy, J. L. 1993, A&AS, 101, 551

—. 1999, A&A, 346, 955

Magalhaes, A. M., Rodrigues, C. V., Margoniner, V. E., Pereyra, A., & Heathcote, S. 1996, in Astronomical Society of the Pacific Conference Series, Vol. 97, Polarimetry of the Interstellar Medium, ed. W. G. Roberge & D. C. B. Whittet, 118–+

Mao, S. A., Gaensler, B. M., Haverkorn, M., Zweibel, E. G., Madsen, G. J., McClure-Griffiths, N. M., Shukurov, A., & Kronberg, P. P. 2010, ApJ, 714, 1170

Martin, P. G. 1971, MNRAS, 153, 279

Mathewson, D. S. & Ford, V. L. 1970, MmRAS, 74, 139

Mathis, J. S. 1986, ApJ, 308, 281

McComas, D. J., Alexashov, D., Bzowski, M., Fahr, H., Heerikhuisen, J., Izmodenov, V., Lee, M. A., Möbius, E., Pogorelov, N. V., Schwadron, N. A., & Zank, G. P. 2012, Science, 000, 0

McComas, D. J., Allegrini, F., Bochsler, P., Bzowski, M., Christian, E. R., Crew, G. B., DeMajistre, R., Fahr, H., Fichtner, H., Frisch, P. C., Funsten, H. O., Fuselier, S. A., Gloeckler, G., Gruntman, M., Heerikhuisen, J., Izmodenov, V., Janzen, P., Knappenberger, P., Krimigis, S., Kucharek, H., Lee, M., Livadiotis, G., Livi, S., MacDowall, R. J., Mitchell, D., Möbius, E., Moore, T., Pogorelov, N. V., Reisenfeld, D., Roelof, E., Saul, L., Schwadron, N. A., Valek, P. W., Vanderspek, R., Wurz, P., & Zank, G. P. 2009, Science, 326, 959

McComas, D. J., Bzowski, M., Frisch, P. C., Crew, G. B., Dayeh, M. A., DeMajistre, R., Funsten, H. O., Fuselier, S. A., Gruntman, M., Janzen, P., Kubiac, M. A., Livadiotis, G., Möbius, E., Reisenfeld, D., & Schwadron, N. A. 2010, J. Geophys. Res., 115, A09113

McComas, D. J., Funsten, H. O., Fuselier, S. A., Lewis, W. S., Möbius, E., & Schwadron, N. A. 2011, Geophys. Res. Lett., 381, 18101

Nagashima, K., Fujimoto, K., & Jacklyn, R. M. 1998, J. Geophys. Res., 103, 17429

Naghizadeh-Khouei, J. & Clarke, D. 1993a, A&A, 274, 968

—. 1993b, A&A, 274, 968

Opal, C. B. & Weller, C. S. 1984, ApJ, 282, 445

Opher, M., Bibi, A., Toth, G., Richardson, J. D., Izmodenov, V. V., & Gombosi, T. I. 2009, Nature, 000, 000

Ostriker, E. C., Stone, J. M., & Gammie, C. F. 2001, ApJ, 546, 980

Perryman, M. A. C. 1997, A&A, 323, L49

Piirola, V. 1973, A&A, 27, 383

—. 1977, A&AS, 30, 213

Pogorelov, N. V., Heerikhuisen, J., Mitchell, J. J., Cairns, I. H., & Zank, G. P. 2009a, ApJ, 695, L31

—. 2009b, ApJ, 695, L31

Prested, C., Opher, M., & Schwadron, N. 2010, ApJ, 716, 550

Rand, R. J. & Kulkarni, S. R. 1989, ApJ, 343, 760

Ratkiewicz, R., Ben-Jaffel, L., & Grygorczuk, J. 2008, in Astronomical Society of the Pacific Conference Series, Vol. 385, Numerical Modeling of Space Plasma Flows, ed. N. V. Pogorelov, E. Audit, & G. P. Zank, 189–+

Ratkiewicz, R., Strumik, M., & Grygorczuk, J. 2012, ApJ, 756, 3

Redfield, S. & Linsky, J. L. 2004a, ApJ, 602, 776

—. 2004b, ApJ, 613, 1004

—. 2008, ApJ, 673, 283

Richardson, J. D. & Stone, E. C. 2009, Space Sci. Rev., 143, 7

Roberge, W. G. 2004, in Astronomical Society of the Pacific Conference Series, Vol. 309, Astrophysics of Dust, ed. A. N. Witt, G. C. Clayton, & B. T. Draine, 467–+

Salvati, M. 2010, A&A, 513, A28+

Santos, F. P., Corradi, W., & Reis, W. 2011, ApJ, 728, 104

Schwadron, N. A., Adams, F. C., Dingus, B., Funsten, H. O., Desiati, P., McComas, D. J., & Frisch, P. C. 2012, ApJ, submitted, 00, 00

Schwadron, N. A., Allegrini, F., Bzowski, M., Christian, E. R., Crew, G. B., Dayeh, M., DeMajistre, R., Frisch, P., Funsten, H. O., Fuselier, S. A., Goodrich, K., Gruntman, M., Janzen, P., Kucharek, H., Livadiotis, G., McComas, D. J., Moebius, E., Prested, C., Reisenfeld, D., Reno, M., Roelof, E., Siegel, J., & Vanderspek, R. 2011, ApJ, 731, 56

Schwadron, N. A., Bzowski, M., Crew, G. B., Gruntman, M., Fahr, H., Fichtner, H., Frisch, P. C., Funsten, H. O., Fuselier, S., Heerikhuisen, J., Izmodenov, V., Kucharek, H., Lee, M., Livadiotis, G., McComas, D. J., Moebius, E., Moore, T., Mukherjee, J., Pogorelov, N. V., Prested, C., Reisenfeld, D., Roelof, E., & Zank, G. P. 2009, Science, 326, 966

Schwarz, D. J., Starkman, G. D., Huterer, D., & Copi, C. J. 2004, Phys. Rev. Let., 93, 221301

Serkowski, K., Mathewson, D. S., & Ford, V. L. 1975, ApJ, 196, 261

Slavin, J. D. & Frisch, P. C. 2008, A&A, 491, 53

Slavin, J. D., Frisch, P. C., Heerikhuisen, J., Pogorelov, N. V., Mueller, H., Reach, W. T., Zank, G. P., Dasgupta, B., & Avinash, K. 2009, Space Science Reviews, (Proceedings of Solar Wind 12). in press (http://adsabs.harvard.edu/abs/2009arXiv0911.1492S)

Slavin, J. D., Frisch, P. C., Mueller, H.-R., Heerikhuisen, J., Pogorelov, N. V., Reach, W. T., & Zank, G. P. 2012, ApJ, submitted

Spoelstra, T. A. T. 1972, A&A, 21, 61

Starkman, G., Copi, C. J., Huterer, D., & Schwarz, D. J. 2009, in Cosmic Structure and Evolution

Stone, E. C., Cummings, A. C., McDonald, F. B., Heikkila, B. C., Lal, N., & Webber, W. R. 2008, Nature, 454, 71

Surdo, A. & Argo-Ybj Collaboration. 2011, Astrophysics and Space Sciences Transactions, 7, 131

Taylor, A. R., Stil, J. M., & Sunstrum, C. 2009, ApJ, 702, 1230

Tilley, D. A., Balsara, D. S., & Howk, J. C. 2006, MNRAS, 371, 1106

Tinbergen, J. 1982, A&A, 105, 53

Welty, D. E. & Crowther, P. A. 2010, MNRAS, 404, 1321

Witte, M. 2004, A&A, 426, 835

Wolleben, M. 2007, ApJ, 664, 349

Wood, B. E., Redfield, S., Linsky, J. L., Müller, H.-R., & Zank, G. P. 2005, ApJS, 159, 118

A.   Appendix: Heliosphere models and the IBEX Ribbon

Heliosphere models predict the density and ionization of the LIC and the ISMF that shapes the heliosphere (e.g. Opher et al. 2009; Pogorelov et al. 2009a; Ratkiewicz et al. 2008; Prested et al. 2010), and originally showed that the Ribbon forms where the sightline is perpendicular to the direction of the interstellar field draping over the heliosphere (Schwadron et al. 2009; Heerikhuisen et al. 2010; Chalov et al. 2010; Grygorczuk et al. 2011; Heerikhuisen & Pogorelov 2011; Ratkiewicz et al. 2012). The exact mechanism generating the Ribbon is a conundrum, partly because the properties of turbulence upstream of the heliopause are unknown (Gamayunov et al. 2010; Florinski et al. 2010), so that several possible scenarios for the formation of the Ribbon have been suggested (e.g. McComas et al. 2010; Schwadron et al. 2011; Grzedzielski et al. 2010). One possible Ribbon formation mechanism requires outflowing ENAs to escape from the heliosphere, and charge exchange with interstellar protons in the outer heliosheath. These ENAs subsequently create secondary inflowing ENAs from another quick charge exchange with interstellar neutrals before the ring-beam distribution of the ions (with a pitch angle of $\sim$ 90°) is disrupted by turbulence, and therefore giving the $B \cdot R = 0$ alignment. Testing for such a model, Heerikhuisen & Pogorelov (2011) varied the strength and direction of the ISMF, and the interstellar neutral H and proton densities, to obtain a best-fit to the geometry of the Ribbon. These models suggest the Ribbon is formed roughly $\sim$ 100 AU beyond the heliopause, by a local ISMF that is directed away from the galactic coordinates $\ell, b = 33° \pm 4°, 53° \pm 2°$, for a field strength of 2–3 μG. For comparison, an earlier MHD

model of the heliosphere asymmetries implied by the deflection of the solar wind in the inner he-
liosheath gave an ISMF direction of $\ell= 10° - 22°$, $b= 28° - 38°$, and field strength $\sim 3.7 - 5.5$
μG (Opher et al. 2009). For the Heerikhuisen & Pogorelov (2011) models, the angle between the
center of the Ribbon arc and the ISMF direction is $\sim 0° - 15°$.

The global heliosphere provides an *in situ* diagnostic of the magnetic field and plasma shaping
the heliosphere. The $\sim 48°$ offset between ISMF direction given by the Ribbon arc center and the
velocity of the inflowing neutral interstellar gas creates asymmetries that can be predicted using
MHD models (e.g. Pogorelov et al. 2009b; Opher et al. 2009; Ratkiewicz et al. 2008; Prested et al.
2010). The data tracing the heliosphere asymmetries include the different distances of the solar
wind termination shock found by Voyager 1 in the northern ecliptic hemisphere and that found
by Voyager 2 in the south (94 AU vs. 84 AU, Stone et al. 2008; Richardson & Stone 2009), the
$\sim 8°$ offset between the upwind directions of the neutral interstellar H^o and He^o flowing into the
heliosphere (using data from Lallement et al. 2010; McComas et al. 2012), and the preferential
alignment exhibited by the 3 kHz plasma emissions from the ISM beyond the heliopause that were
detected by both Voyagers (e.g. Kurth & Gurnett 2003). The ISMF directions from these models
are generally consistent with the field direction from the IBEX ribbon.

McComas et al. (2012) have determined a new consensus direction for the velocity vector of
interstellar He^o flowing through the heliosphere. The He^o gas velocity, 23.2 ± 0.3 km s^{-1} (Table
1), agrees with the (less precise) velocity of interstellar dust traveling through the heliosphere,
after correction for propagation effects, of $24.5^{+1.1}_{-1.2}$ km s^{-1} from galactic coordinates ℓ,$b= 8° \pm$
$15°, 14° \pm 4°$ (Frisch et al. 1999; Kimura et al. 2003). It also agrees with the velocity of interstellar
H^o interacting with the heliosphere found from the first spectrum of Lyα emission from interstellar
H^o inside of the heliosphere, 22.5 ± 2.8 km s^{-1}, after correction for H^o propagation and to the
consensus IBEX upwind direction (Adams & Frisch 1977).

The outer boundary conditions of the heliosphere models are set by the physical properties
of the LIC, which must be reconstructed from ISM observations using photoionization models be-
cause of the low opacity of the cloud. Ribbon models are highly sensitive to the interstellar bound-
ary conditions of the heliosphere; 15% variations in the interstellar parameters lead to pronounced
differences in the location and width of the Ribbon (Frisch et al. 2010b). Photoionization models
indicate that the LIC is a low density, $n \sim 0.27$ cm^{-3}, partially ionized cloud, $H^+/H \sim 22\%$ and
$He^+/He \sim 39\%$ (Model 26 in Slavin & Frisch 2008). Observations of ISM inside of the helio-
sphere also probe the LIC properties. When the IBEX measurements of interstellar O^o, and Ne^o are
corrected for propagation effects through and entering the heliosphere, and ionization in the LIC
using photoionization models, the interstellar abundance ratio O/Ne$= 0.27 \pm 0.10$ that is recovered
agrees with other local ISM measurements and suggests that over 50% of the O is depleted onto
interstellar dust grains (Bochsler et al. 2012). IBEX and Ulysses measurements of interstellar He^o

indicate the LIC is warm, 6300 ± 390 K (Witte 2004; McComas et al. 2012).

New IBEX-LO observations of the flow of interstellar He^o through the inner heliosphere (McComas et al. 2012) indicate that ISM flow is $\sim 12\%$ slower than found from earlier Ulysses data (Witte 2004), which lowers the interstellar ram pressure on the heliosphere by $\sim 22\%$ and may affect the models of the Ribbon location. The value of the He^o flow vector is given in Table 1, together with the 1σ uncertainties for longitude, latitude, and velocity. The new IBEX upwind direction has shifted to $3.6°$ east of the Ulysses direction. The uncertainties are somewhat larger when the bounding range constrains are included; these constraints set the limits as $\ell = 5.25^{+1.48}_{-1.37}$ degrees, $b = 12.03^{+2.67}_{-3.19}$ degrees, the velocity to $-23.20^{+2.5}_{-1.9}$ km s^{-1}, and the temperature to 5000–8300 K.

B.   Appendix: List of stars from the literature included in study

The stars within 40 parsecs from the PlanetPol catalog included in this study are: HD 97603 (HR 4357), HD 140573 (HR 5854), HD 139006 (HR 5793), HD 116656 (HR 5054), HD 156164 (HR 6410), HD 95418 (HR 4295), HD 112185 (HR 4905), HD 161096 (HR 6603), HD 177724 (HR 7235), HD 127762 (HR 5435), HD 153210 (HR 6299), HD 120315 (HR 5191), HD 113226 (HR 4932), HD 112413 (HR 4915), HD 163588 (HR 6688), HD 95689 (HR 4301) and HD 131873 (HR 5563).

The nearby stars from Santos et al. (2011) catalog that have been used in this study include: HD 223889 (HIP 117828), HD 120467 (HIP 67487), HD 173818 (HIP 92200), HIP 65520, HD 127339 (HIP 70956), HIP 82283, HIP 50808, HIP 106803, HD 162283 (HIP 87322), HIP 114859 HIP 83405 HIP 96710 HIP 90035 HIP 87745 HD 176986 (HIP 93540), HD 175726 (HIP 92984), HIP 61872, HIP 95417, HD 155802 (HIP 84303), HD 166184 (HIP 88961), HD 161098 (HIP 86765), HD 182085 (HIP 95299), HD 164651 (HIP 88324), HD 119638 (HIP 67069), HD 125184 (HIP 69881), HD 95521 (HIP 53837), HIP 66918, HD 177409 (HIP 94154), HD 144660 (HIP 78983), HD 151528 (HIP 82260), HD 95338 (HIP 53719), HD 127352 (HIP 70973), HD 183063 (HIP 95722), HD 105328 (HIP 59143), HD 204385 (HIP 106213), HD 145809 (HIP 79524), HD 172675 (HIP 91645), HD 149013 (HIP 81010), HD 185615 (HIP 96854) and HD 138885 (HIP 76292).

The seven PlanetPol stars that define the upper end of the region $RA = 16^H - 20^H$ polarization envelope (§5.3) are listed in Table 3.

C.   Polarization vrs Distance relation

Polarization of optical starlight in the interstellar medium is due to magnetically aligned dichroic dust grains, so that there is a correlation between the upper envelope of polarization and interstellar extinction for a given set of observations (Serkowski et al. 1975; Fosalba et al. 2002; Andersson 2012). The usual term "upper envelope" describes the relation between the maximum observed polarizations for a set of stars as a function of extinction, i.e. for a given extinction no polarization is found above the upper envelope value by definition. Figure 7 shows that an upper envelope is also present in the polarization-distance plot. The scatter of polarization strengths for a given extinction is due to the patchy nature of the ISM and magnetic turbulence. Likewise, the presence of an upper envelope to the polarization-distance plot in Figure 7 likely results from either the patchy nature of nearby ISM (Frisch et al. 2011), or magnetic turbulence, or both.

The polarization data represented in Figure 3 were collected over a timespan of a half of a century, using a diverse set of instruments with unknown systematics. The reasonableness of the statement that polarization increases with distance has been tested for the stars shown in the figure using the nonparametric Kendall's tau measure of bivariate correlation. For the set of stars where Pol/dPol≥ 3, the rank correlation coefficiet is $\tau = 0.86$, where a value of one indicates that there is a perfect association of increasing polarization with increasing distance. Selecting only the most accurate data points, Pol/dPol≥ 5, yields $\tau = 0.89$. However for the nearest stars used in this analysis, < 40 pc, this association is not demonstrated ($\tau = 0.14$ $P/dP \geq 3$), an effect that we attribute both to influence of systematic uncertainties on weak polarization measurements and to the patchy nature of nearby ISM. In §5.3.1 we discuss a special nearby region where increasing interstellar polarization is shown to be associated with increasing distance for stars within 40 pc.

D.   Asymmetry of very local interstellar radiation field

The asymmetry of the local interstellar radiation field is related to the overall opacity of the Local Bubble. The brightest of the far-UV sources are located in the third and fourth galactic quadrants ($\ell = 180° - 360°$, Gondhalekar et al. 1980) because of the distribution of massive stars with respect to the Local Bubble void. Those same stars are bright at the 13.6 eV ionization edge of H^{o} so that in the absence of interstellar opacity the $\ell = 180° - 360°$ interval will be more highly ionized (Frisch 2010). This distribution of radiation sources explains the relation between polarization and the radiation field at each star that is displayed in Figure 9.

Figure 12 shows the different levels of far UV radiation at 975 Å between galactic quadrants I and II ($\ell = 0° - 180°$) and III and IV ($\ell = 180° - 360°$). The sum of the stellar fluxes are shown at spherical surfaces around the Sun with radii of 25 parsecs and 45 parsecs, and displayed using

an aitoff projection. The mapped fluxes represent the sum of stellar fluxes at each position, based on the twenty-five brightest OB stars at 975 Å (Opal & Weller 1984). Flux units are photons cm^{-2} s^{-1} $Å^{-1}$. The fluxes are plotted with the same color-coding in both figures. The minimum and maximum flux values on the color bar correspond to 4.0×10^4 and 8.0×10^4 cm^{-2} s^{-1} $Å^{-1}$, respectively. Low radiation fluxes in the region of large PlanetPol polarizations are the result of the locations of hot stars.

Table 1. Various Directions

Source coordinates	Longitude deg.	Latitude deg.	Notes (and references)
Direction of best-fitting Magnetic Field			
Polarization, Paper I, unweighted:			
Ecliptic	263	37	uncertainties ± 35
Galactic	37	23	uncertainties ± 35
Polarization, this Paper, unweighted:			
Ecliptic	263^{+10}_{-5}	37 ± 15	
Galactic	37 ± 15	22 ± 15	
Polarization, this Paper, weighted:			
Ecliptic	263^{+15}_{-20}	47 ± 15	
Galactic	47 ± 20	25 ± 20	
ISMF from Center of Ribbon arc:			[2]
Ecliptic	221 ± 4	39 ± 4	(see text)
Galactic	33 ± 4	55 ± 4	
Upwind direction of interstellar He^o flow through heliosphere		V=23.2 ± 0.3 km s^{-1}, T= 6300 ± 390 K [1]	
Ecliptic	259.00 ± 0.47	4.98 ± 0.21	
Galactic	5.25 ± 0.24	12.03 ± 0.51	
Quadrant III pulsars			
Ecliptic	232	18	[6]
Galactic	5	42	[6]
Heliotail in globally distributed IBEX ENA flux			
Ecliptic	30 ± 30	0 ± 30	[5]
Galactic	146 ± 30	-49 ± 30	[5]
Direction of tail-in cosmic ray asymmetries			
Sub-TeV anisotropies:			
Ecliptic	90	-47	cone half-width=68 [3]
Galactic	230	-21	cone half-width=68 [3]
Ecliptic	66	-36	center of Gaussian fit [4]
Galactic	211	-35	center of Gaussian fit [4]

References. — [1] McComas et al. (2012) [2] Funsten et al. (2009) [3] Nagashima et al. (1998) [4] Hall et al. (1999) [5] Schwadron et al. (2011) [6] Salvati (2010)

Table 2.   New LNA and NOT Polarization Data

HD	ℓ deg	b deg	Dist. pc	Pol 10^{-5}	PA_{cel} deg	PA_{gal} deg	Source
1581	309	-53	8	15 ± 16	73 ± 52	60 ± 52	LNA
2025	32	-83	18	142 ± 88	125 ± 17	34 ± 17	LNA
3443	69	-84	15	19 ± 13	138 ± 52	2 ± 52	LNA
4628	120	-57	7	7 ± 11	86 ± 52	88 ± 52	LNA
5133	297	-87	14	45 ± 73	75 ± 52	72 ± 52	LNA
7570	290	-71	15	41 ± 14	70 ± 9	86 ± 9	LNA
10360	289	-59	8	22 ± 11	158 ± 14	179 ± 14	LNA
14412	209	-70	12	8 ± 17	28 ± 52	131 ± 52	LNA
16160	162	-48	7	20 ± 15	131 ± 52	95 ± 52	LNA
23356	210	-50	14	449 ± 53	7 ± 3	117 ± 3	LNA
125072	313	2	11	29 ± 135	156 ± 52	174 ± 52	LNA
129502	346	47	18	3 ± 3	110 ± 24	148 ± 24	NOT
130819	340	38	23	6 ± 3	81 ± 14	114 ± 14	NOT
131923	323	10	24	47 ± 24	41 ± 14	68 ± 14	LNA
131976	338	33	7	63 ± 65	30 ± 52	63 ± 52	LNA
131977	338	33	5	55 ± 24	66 ± 12	99 ± 12	LNA
134987	339	27	25	14 ± 2	65 ± 4	100 ± 4	NOT
136894	340	24	28	14 ± 4	70 ± 8	106 ± 8	NOT
141272	369	40	21	63 ± 32	56 ± 13	110 ± 13	KVA
144253	352	23	18	13 ± 3	69 ± 7	115 ± 7	NOT
144585	358	27	28	2 ± 2	56 ± 23	104 ± 23	NOT
152311	0	14	28	3 ± 3	39 ± 20	91 ± 20	NOT
153631	7	17	26	5 ± 3	6 ± 13	61 ± 13	NOT
154088	355	7	18	6 ± 3	60 ± 11	113 ± 11	NOT
156897	3	8	17	5 ± 3	127 ± 13	3 ± 13	NOT
160346	27	18	10	30 ± 28	173 ± 52	55 ± 52	LNA
161096	29	17	25	5 ± 0	166 ± 0	49 ± 0	Wik
165222	24	9	7	17 ± 18	23 ± 52	84 ± 52	LNA
167665	4	-5	29	4 ± 3	113 ± 16	174 ± 16	NOT
169916	7	-6	23	7 ± 3	109 ± 12	171 ± 12	NOT
169916	7	-6	24	36 ± 7	109 ± 7	172 ± 7	KVA
170657	13	-4	13	4 ± 3	66 ± 18	128 ± 18	NOT
172051	12	-6	13	2 ± 3	110 ± 26	173 ± 26	NOT
176029	38	1	11	25 ± 23	141 ± 52	23 ± 52	LNA
177716	9	-15	37	38 ± 7	113 ± 7	179 ± 7	KVA

Table 2—Continued

| HD | ℓ | b | Dist. | Pol | PA$_{cel}$ | PA$_{gal}$ | Source |
	deg	deg	pc	10^{-5}	deg	deg	
178428	49	4	21	2 ± 3	63 ± 23	125 ± 23	NOT
179949	13	-15	27	10 ± 3	77 ± 7	144 ± 7	NOT
180409	25	-10	28	4 ± 2	95 ± 16	159 ± 16	NOT
180409	27	-9	28	23 ± 14	50 ± 16	113 ± 16	LNA
180617	40	-2	5	37 ± 82	25 ± 52	87 ± 52	LNA
184489	41	-7	14	7 ± 16	73 ± 52	135 ± 52	LNA
184509	18	-18	31	7 ± 3	108 ± 11	175 ± 11	NOT
184985	25	-16	30	8 ± 3	88 ± 9	153 ± 9	NOT
186427	83	13	21	5 ± 2	111 ± 9	174 ± 9	NOT
188088	18	-22	14	10 ± 12	138 ± 52	26 ± 52	LNA
189245	8	-27	20	38 ± 12	144 ± 9	37 ± 9	LNA
189340	33	-18	24	28 ± 21	166 ± 52	50 ± 52	LNA
189931	4	-29	27	17 ± 16	108 ± 52	3 ± 52	LNA
191408	5	-30	6	15 ± 35	65 ± 52	141 ± 52	LNA
191849	355	-32	6	16 ± 5	167 ± 8	69 ± 8	LNA
191862	30	-23	28	1 ± 3	112 ± 34	178 ± 34	NOT
192310	15	-28	8	36 ± 21	156 ± 16	48 ± 16	LNA
194640	13	-32	19	47 ± 1760	17 ± 52	91 ± 52	LNA
194943	26	-29	30	1 ± 3	170 ± 35	58 ± 35	NOT
196761	22	-32	14	25 ± 18	128 ± 52	19 ± 52	LNA
202560	6	-43	3	10 ± 32	89 ± 52	175 ± 52	LNA
207129	351	-48	15	32 ± 9	93 ± 8	14 ± 8	LNA
211415	340	-51	13	13 ± 5	41 ± 10	156 ± 10	LNA
213042	18	-58	15	18 ± 18	108 ± 52	14 ± 52	LNA
222237	311	-44	11	86 ± 97	52 ± 52	28 ± 52	LNA

Table 3.   PlanetPol* stars in polarization envelope

HD	hame	Coordinates deg	Distance pc	Polarization ppm	PA$_{RA}$ deg
172167	α Lyr	67.4, 19.2	7.8	17.2 ± 1.1	34.5 ± 1.4
159561	α Oph	35.9, 22.6	14.3	23.4 ± 2.0	30.8 ± 2.4
161868	γ Oph	28.0, 15.4	29.1	40.8 ± 3.1	28.5 ± 2.1
164058	γ Dra	79.1, 29.2	45.2	73.3 ± 1.2	145.0 ± 0.5
186882	$\cdots$	78.7, 10.2	52.4	108.0 ± 2.0	22.8 ± 0.5
168775	$\cdots$	63.5 , 21.5	70.4	106.5 ± 2.7	6.1 ± 0.7
189319	$\cdots$	58.0 , –5.2	84.0	199.5 ± 1.4	56.1 ± 0.2

*Bailey et al. (2010)
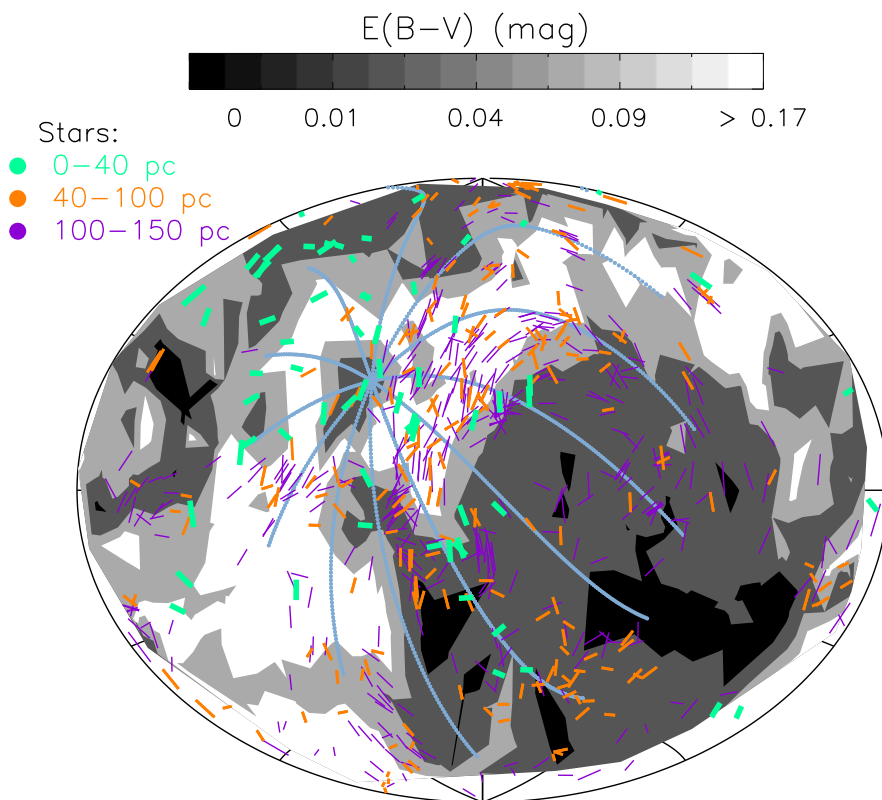
Fig. 1.— The configuration of the ISM associated with Loop I is displayed. Filled contours show interstellar dust 100 within parsecs and the short lines show interstellar polarization directions. The extended gray-blue curved lines show the best-fitting ISMF for the region within 40 pc and 90° of the heliosphere nose (§4.2, Table 1). Star distance is coded as follows: within 40 pc (cyan blue), 40–100 pc (orange) and 100–150 pc (purple). Line length is unrelated to polarization strength. The Loop I ISMF direction is clearly defined by the polarizations of distant stars (e.g. Santos et al. 2011), but also appears to extend close to the Sun (§5.3). The lightest contours show maximum dust color excess values, E(B–V), while the darkest regions with E(B–V)≤ 0.01 mag show that the interior void of the Loop I bubble extends to the Sun location. The color excess E(B–V) contours are based on the photometric and astrometric data for stars brighter than V=9 mag in the Hipparcos catalog (Perryman 1997) and the absolute stellar colors in Cox (2000); E(B–V) values are then smoothed spatially over $\sim \pm 13°$ intervals for overlapping distances (considering uncertainties). Variable stars with δV ≥ 0.06 mag, as indicated by the Hipparcos variability index H6, have been omitted. The E(B–V) contour levels of 0.01, 0.04, 0.09, 0.17 mag correspond to column densities $\log(N(\mathrm{H^o}+H_2))$ of 19.76, 20.37, 20.72, and 20.99 cm^{-2}, for $N(\mathrm{H^o}+H_2)/E$(B–V)= 5.8×10^{21} atoms cm^{-2} mag-1 (Bohlin et al. 1978). Note the third and fourth quadrant voids (dark region between $\ell \sim 210°$–0°) compared to the nearby brightest interstellar radiation field (Appendix D). The figure is centered on the galactic center, with longitude increasing towards the left. The polarization data are from the sources listed in §3 and Heiles (2001).
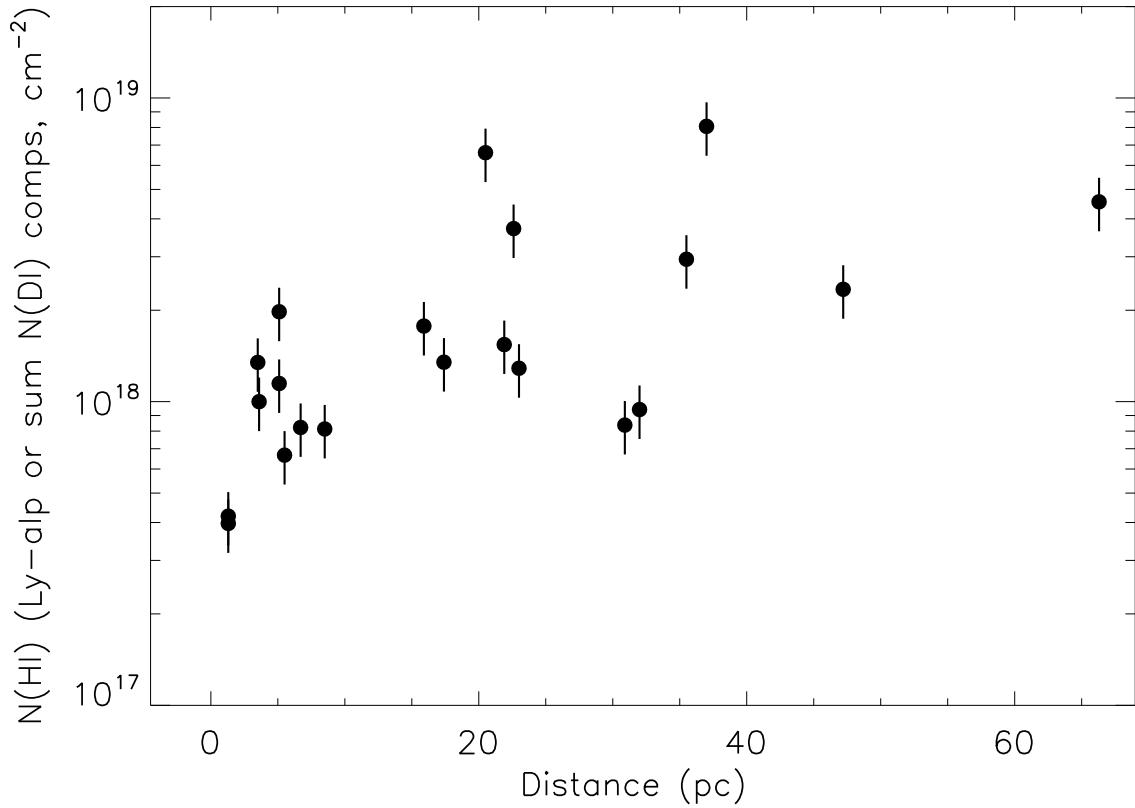
Fig. 2.— Column densities are plotted as a function of distance toward nearby stars within 40 pc and $90°$ of the heliosphere nose. The H^o column density is found from either Lyα data (Wood et al. 2005), or the the sum of D^o components using D^o/H^o= 1.5×10^{-5} (Redfield & Linsky 2004a). The uncertainties are plotted as 20% of the column density.
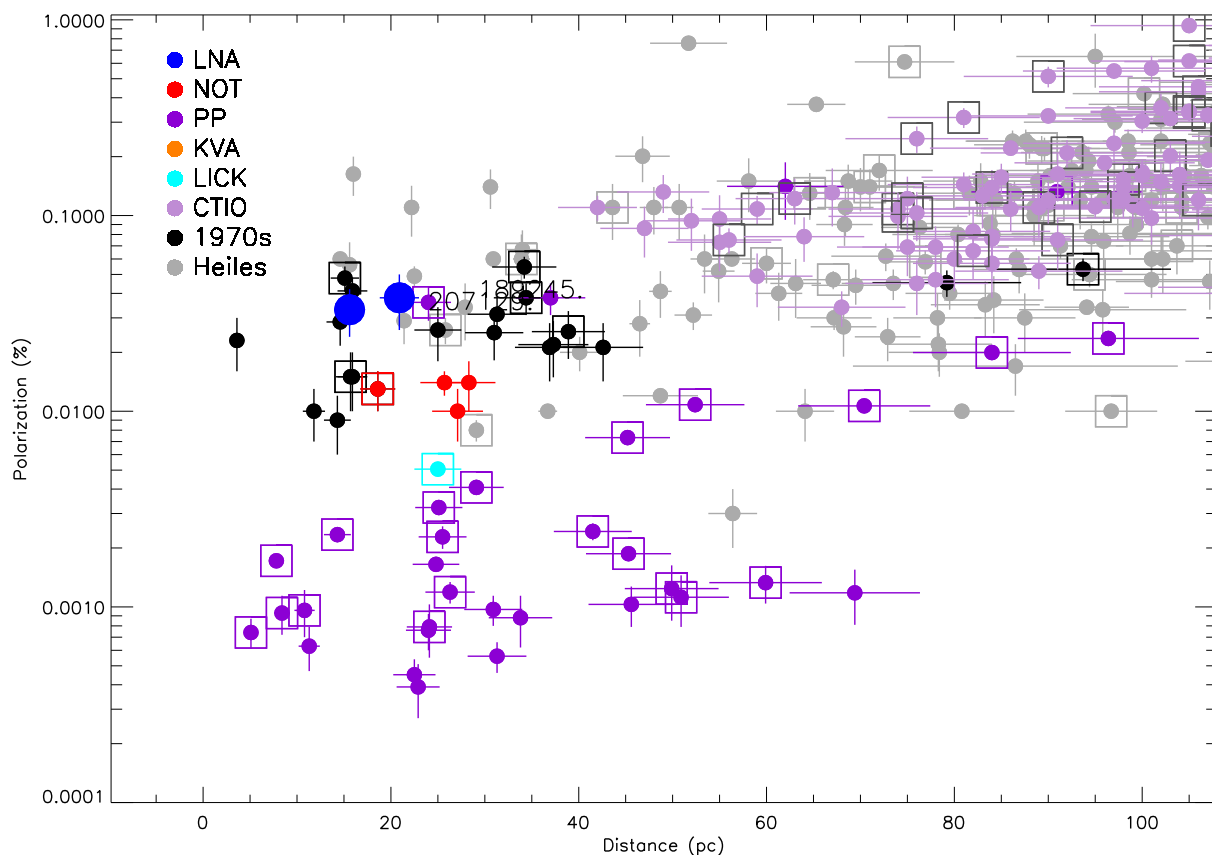
Fig. 3.— Interstellar polarizations with $P/dP > 3.0$, and for stars within $90°$ of the heliosphere nose, are plotted as a function of distance. Data sources are color-coded, according to the scheme in the figure. Dark purple points are the PlanetPol data. The boxes indicate stars in region $RA = 16^H - 20^H$ where Bailey et al. (2010) found that polarizations increase with distance. This region overlaps the North Polar Spur region, which forms the tangential sections of Loop I. PlanetPol requires bright stars to achieve high accuracy, which suggests that systematically lower PlanetPol polarizations beyond 40 pc (and perhaps closer) may be due to selection effects related to the patchiness of foreground dust. Data are from Table 2, the references listed in §3, and Heiles (2000). These data were collected over a variety of wavelength ranges (§3), and differences in polarization strengths will occur because of the wavelength dependence of polarization (Serkowski et al. 1975).
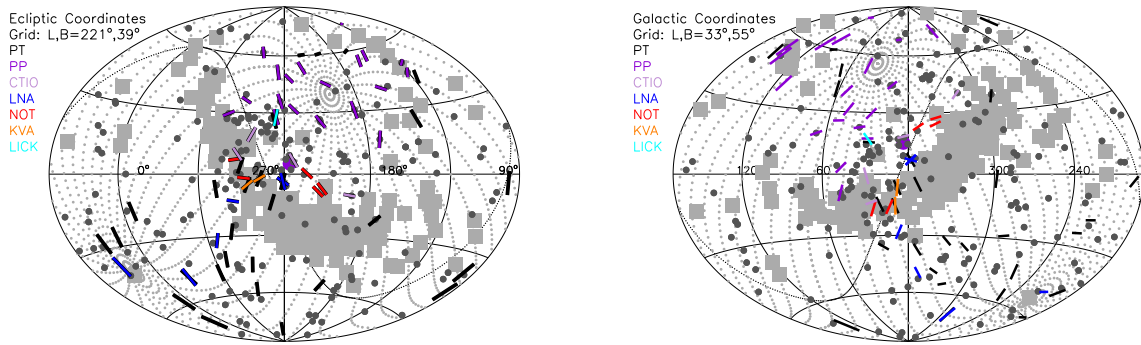
Fig. 4.— The polarization vectors of stars within ~ 40 pc are shown in both ecliptic and galactic coordinate systems, and color-coded for the data source, as indicated in the figure legend. The polarization data are from this paper (LNA and NOT, §3), PlanetPol (Bailey et al. 2010, PP), Paper I (LICK, KVA), (Santos et al. 2011, CTIO), and 20th century data (Piirola 1977; Tinbergen 1982, PT). Both plots are centered close to the heliosphere nose located at ecliptic coordinates (purple circle) of λ=259°, β=5°; longitude increases towards the left. Data with $P/dP< 2.5$ are plotted as dots, and vector lengths do not indicate polarization strength. The Compton-Getting corrected ENA fluxes at 1 keV are plotted for directions where the ENA count rates are larger than 113 counts cm^{-2} s^{-1} sr^{-1} keV^{-1}, which is ~ 1.5 times the mean ENA flux at 1 keV as measured by the IBEX-HI instrument (McComas et al. 2009). The grid of dotted lines show the ISMF determined from the center of the Ribbon arc (Funsten et al. 2009, Table 2).
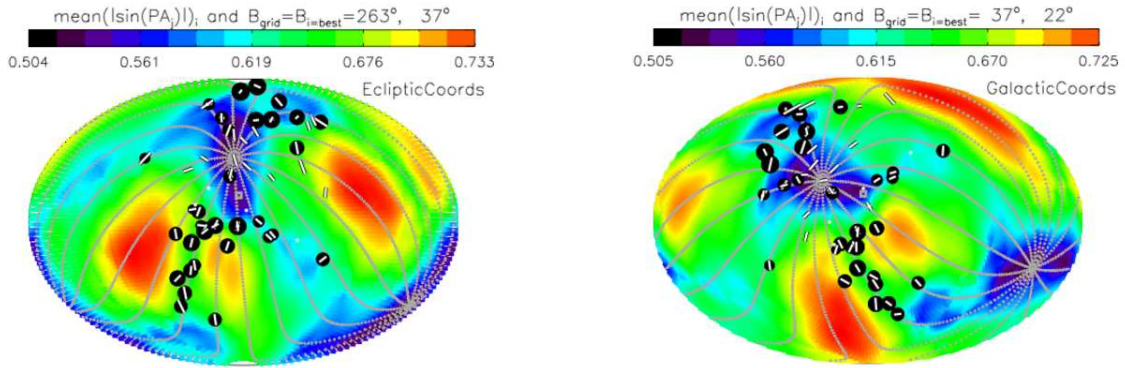
Fig. 5.— The value of the function $F_i = \overline{sin(\theta_{n,i})}$ for the unweighted fit (G_n=1, eqn. 1) is plotted over a regular grid of i possible interstellar field directions, based on unweighted position angles (§4.1). The function is color-coded and plotted in the ecliptic coordinates (left) and galactic coordinates (right), with the left plot centered on the ecliptic nose at $\lambda \sim 259°$, and the right plot centered on the galactic center ($16°$ from the ecliptic nose). The gray dotted grid shows the best-fitting ISMF direction for the unweighted fit listed at the top of the figures (Table 1). Stellar polarization vectors are shown superimposed on black dots for visual clarity.
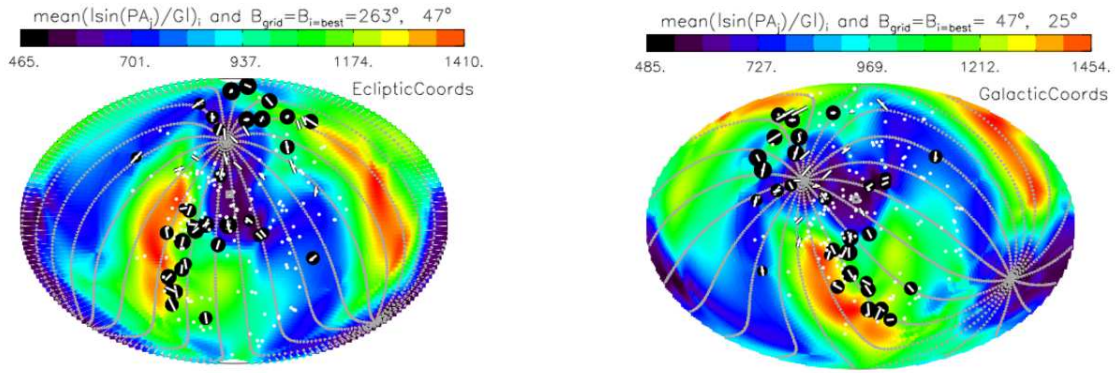
Fig. 6.— The value of the function $F_i' = \overline{sin(\theta_{n,i})/G_n}$ (eqn. 1) evaluated over a regular grid of i possible interstellar field directions, based on weighted position angles with G_n given by eqn. 2. The symbol size is coded to increase with polarization strength, and the dots represent stars where the observed polarization is not statistically significant. The function is color-coded and plotted in ecliptic (left) and galactic (right) coordinates. The gray dotted grid shows the best-fit ISMF direction given at the top of the figures (Table 1). The secondary weaker minimum centered near the heliosphere nose, at plot centers, is dominated by the randomly distributed position angles contributed by low significance data points. See Figure 5 for additional information.
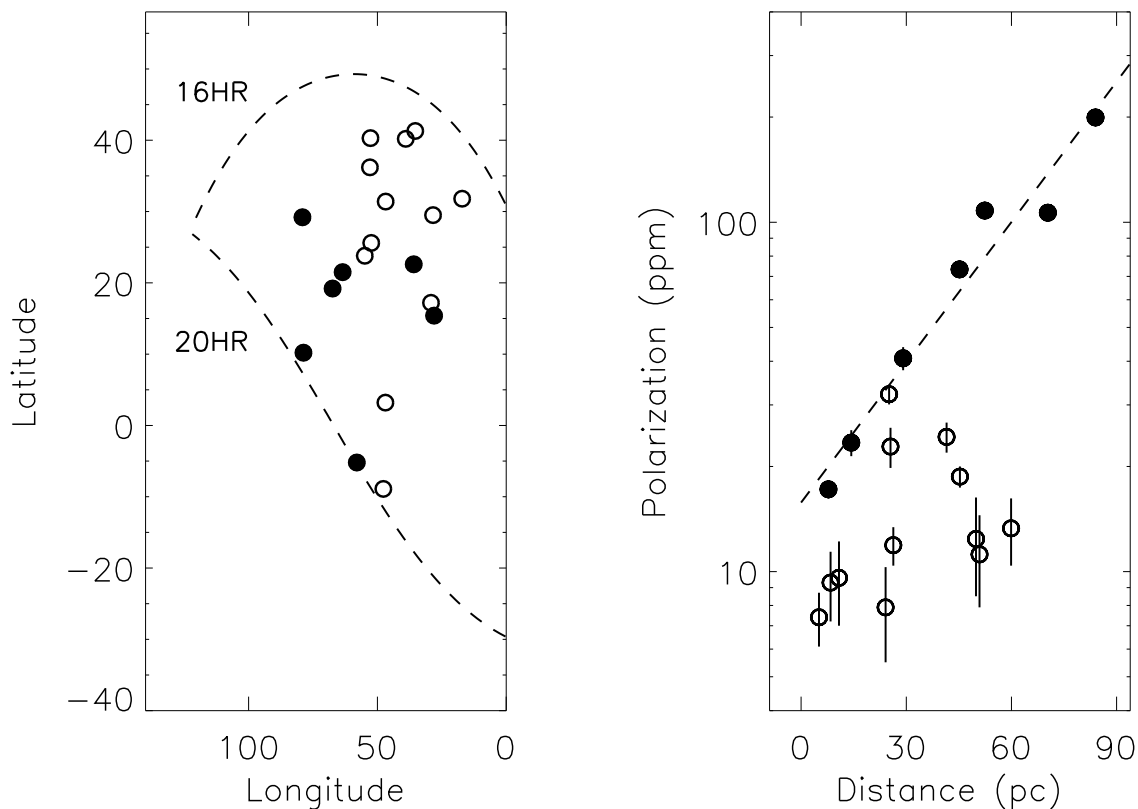
Fig. 7.— Right: The polarizations of the PlanetPol stars with $P/dP > 3.0$, distance $D < 94$ pc, and inside the RA $= 16^{\text{H}} - 20^{\text{H}}$ region are plotted as a function of distance (see text). The upper envelope of the increase of polarization with distance is shown by the filled circles. This upper envelope is analogous to the increase of polarization with color excess (Serkowski et al. 1975). A linear fit to the seven stars in the upper envelope (listed in Appendix B) yields $\log P = 1.200 + 0.013 * D$, where P is in ppm and D is in parsecs. Left: The positions of these stars are plotted in galactic coordinates.
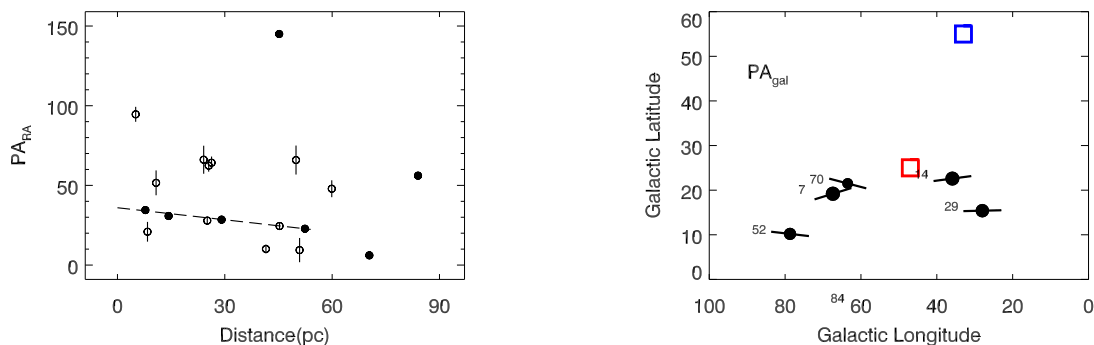
Fig. 8.— Left: Polarization position angles (PA$_{\mathrm{RA}}$) in equatorial coordinates are plotted against the star distance for the PlanetPol data in the RA $= 16^{\mathrm{H}} - 20^{\mathrm{H}}$ region. Filled circles indicate the seven stars that form the upper envelope of the polarization envelope (Figure 7, right). Except for the outlier data point HD 164058 (at 45 pc, PA$_{\mathrm{RA}}$=145°, §5.3), the polarization position angles of the envelope stars vary smoothly for the stars within 55 pc. A linear fit was made to the position angles of envelope stars within 55 pc, excluding the outlier HD 164058. The result is PA$_{\mathrm{RA}}$= A $-$ B $\cdot$ D$_{\mathrm{pc}}$, where A=35.97 $\pm$ 1.41, B= 0.252 $\pm$ 0.030, $\chi^2 = 0.559$ and D_{pc} is the distance in parsecs. The probability that the χ^2 value is larger than 0.559 by chance is 0.76, indicating that a line provides a satisfactory fit to the position angles of the nearest envelope stars. A measure of magnetic turbulence is provided by the 23° standard deviation of the position angles of all stars within 55 pc, excluding the outlier, with respect to the linear fit to the nearest envelope stars. Right: Polarization position angles rotated into galactic coordinates are plotted at the locations of the envelope stars within 70 pc (except for the outlier). Data are labeled by the star distance (Table 3). The best-fitting ISMF from the weighted fit (red box) and the center of the IBEX Ribbon arc (blue box) are plotted for comparison. Uncertainties on the position angles are negligible. Note that the position angle of the closest star HD 172167, 8 pc, is directed towards the best-fitting ISMF.
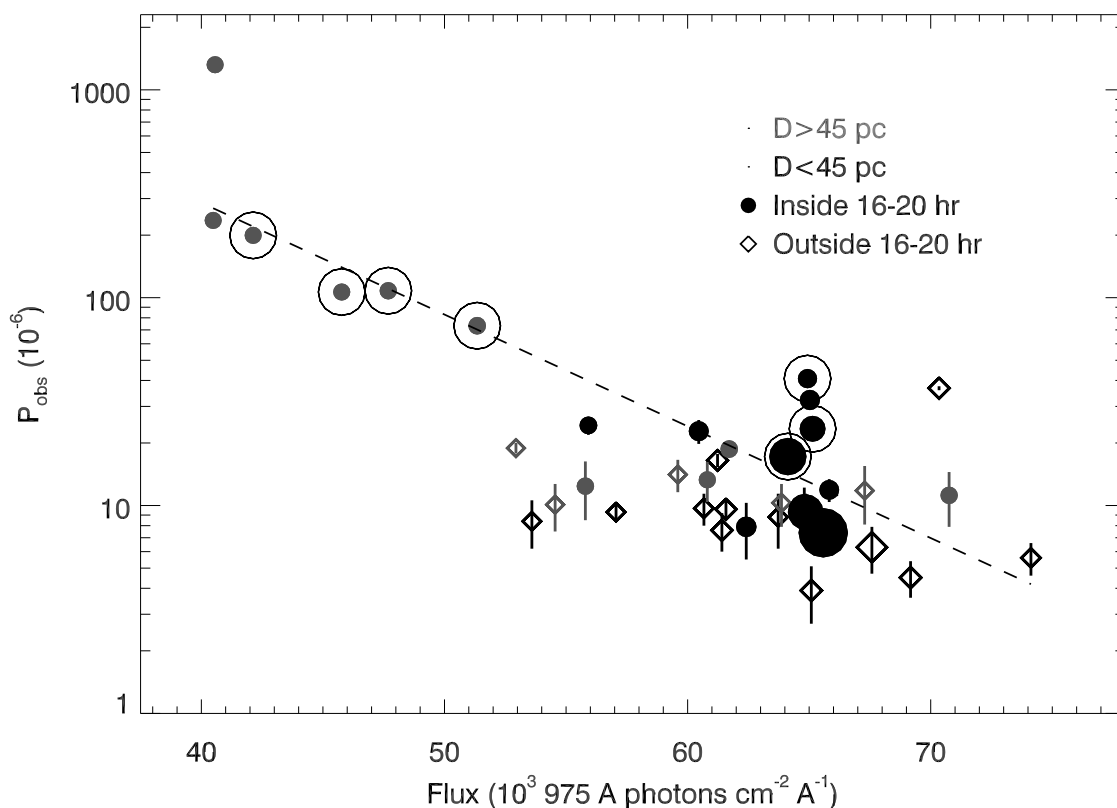
Fig. 9.— Stellar polarizations with 3σ detections are plotted against the FUV radiation field at each star for the 975 Å fluxes from the 25 brightest stars measured by Opal & Weller (1984). Dots show stars in the $\mathrm{RA} = 16^H - 20^H$ region, and diamonds show stars outside of this region. Black/gray symbols indicate stars within/beyond 45 pc. Symbol sizes are inversely proportional to the distance of the star. The seven envelope stars in Figure 7 are circled. The dashed/dotted lines show fits between the polarizations and 975 A fluxes for stars inside/outside of region $\mathrm{RA} = 16^H - 20^H$. Polarization increases strongly at low FUV fluxes, but the effect is probably due to the relative locations of the most polarized distant stars in the first galactic quadrant, and the bright FUV sources that are mainly located in the third galactic quadrant (see Appendix D).
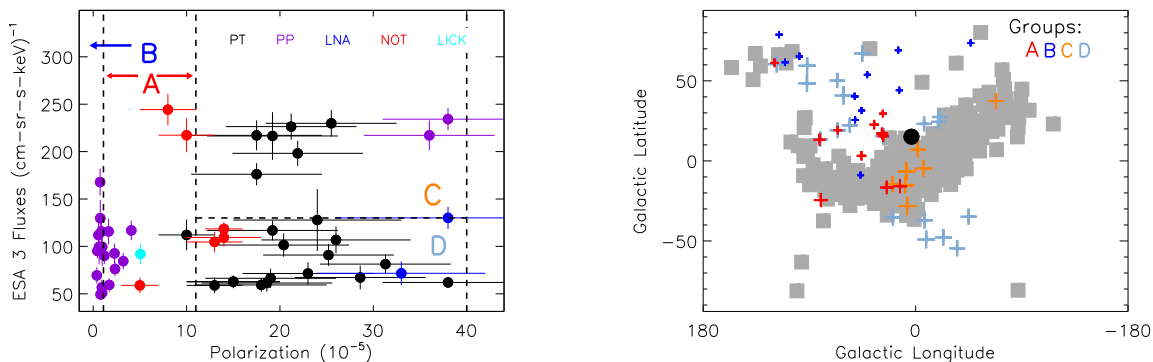
Fig. 10.— Polarization strengths tend to increase with the ENA fluxes for the polarizations with the highest statistical significance. Left: The abscissa shows the polarization for stars within 40 pc and $90°$ of the heliosphere nose, for $P/\sigma > 2.5$ where P, σ are the polarization and 1σ uncertainty. The ordinate shows the mean IBEX-HI 1.1 keV ENA fluxes towards the same stars, where the IBEX fluxes are calculated as the average value for pixels that have S/N> 3.5 and are within 6 degrees of the star. The polarization sources are identified by color, with PT (black) representing 20th century data, PP (purple) representing PlanetPol data, and LNA, NOT, and LICK data representing data acquired for this study (blue, red, cyan, see §3). The data shown in the left figure are divided into four groups, denoted by A, B, C, and D, given by (A) $1 \times 10^{-5} < P < 11 \times 10^{-5}$, all ENA flux levels;(B) $P < 1 \times 10^{-5}$, all ENA flux levels; (C) $11 \times 10^{-5} < P < 40 \times 10^{-5}$ and ENA fluxes > 130; (D) $11 \times 10^{-5} < P < 40 \times 10^{-5}$ and ENA fluxes < 130. The ENA fluxes increase with polarization strength for stars in group A. PlanetPol stars in group A are located in the $\mathrm{RA} = 16^{\mathrm{H}} - 20^{\mathrm{H}}$ region. Right: Stars in the four groups are overplotted on the IBEX Ribbon (1 keV), and color-coded according to the group in the left figure: red=A, B=blue, C=orange, and D=light-blue. Symbol size is proportional to polarization strength. The polarizations in groups A and B are recent data with lower uncertainties; group A in particular shows polarization increasing with ENA fluxes. The light-blue data points (group D) tend to be older data with large uncertainties.
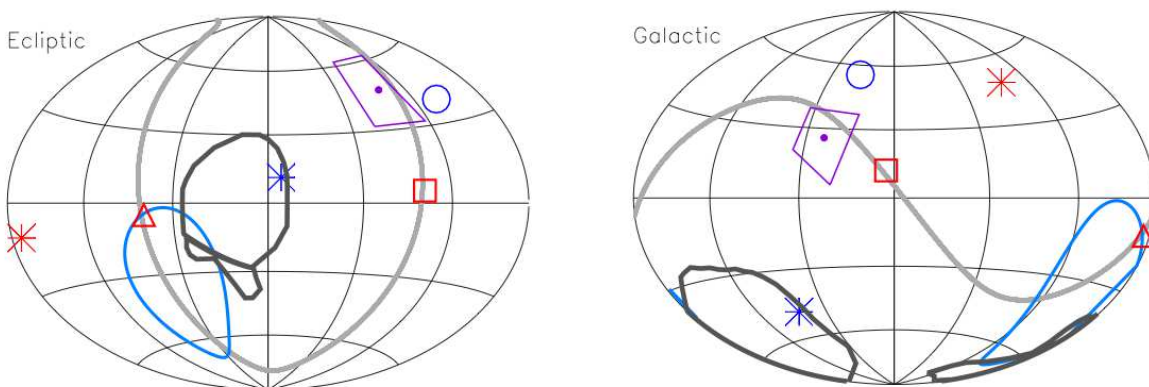
Fig. 11.— The great circle (gray line) in the sky that evenly separates the hot (red asterisk) and cold (blue asterisk) poles of the cosmic microwave background dipole anisotropy is plotted in ecliptic (left) and galactic (right coordinates). The best-fitting ISMF is shown in purple on each plot, with the dot/polygon giving the direction/uncertainties of the weighted fit in Table 1. The great circle equidistant between the CMB dipoles intersects both the best-fitting local ISMF direction and the heliosphere nose (red square, see Table 1), to within the uncertainties. The blue open circle gives the ISMF direction derived from the center of the IBEX Ribbon arc. The large blue circular region (light gray) shows the location of the tail-in anisotropy for ~ 500 GCRs GeV modeled by Hall et al. (1999), with the extent defined by the $68°$ width from Nagashima et al. (1998). The regions outlined by thick black lines show the observed heliotail that is deflected $\sim 44°$ to the west of the downwind gas direction (red triangle), and is prominent in maps of the globally distributed ENAs (Schwadron et al. 2011). Each plot is centered on the longitude of $0°$ in the respective coordinate system, with longitude increasing towards the left.
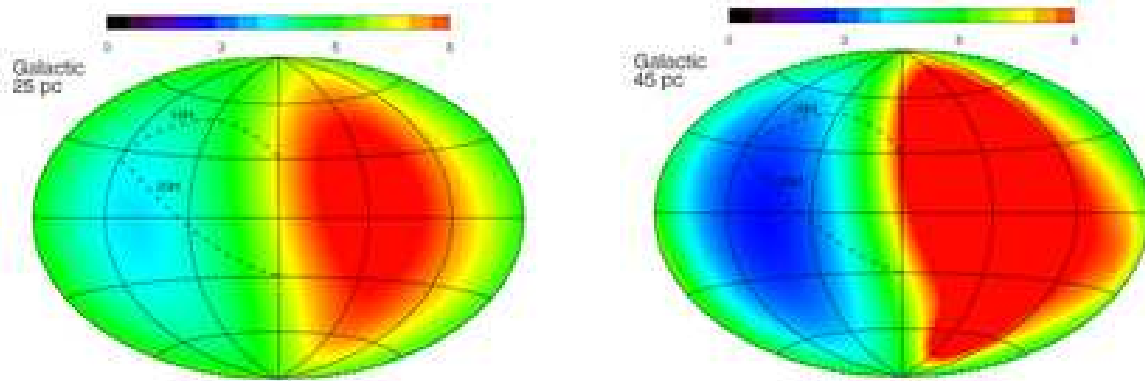
Fig. 12.— Diffuse interstellar fluxes at 975 Å are plotted for spheres of radius 25 pc (left) and 45 pc (right) around the Sun. The figure is centered on the galactic center with galactic longitude increasing towards the left. These fluxes are calculated from the combined fluxes of the 25 brightest stars in the sky at 975 Å based on the measurements of Opal & Weller (1984). Most of that flux originates in the third and fourth galactic quadrants (Gondhalekar et al. 1980), which leads to the strong radiation fluxes in quadrants III and IV (right figure, $\ell > 180°$) when compared to weak fluxes in quadrants I and II ($\ell < 180°$). This asymmetry in the diffuse interstellar radiation field is due to the distribution of massive stars around the Local Bubble void. The more distant stars in the $RA = 16^H - 20^H$ interval are exposed to a lower ambient interstellar radiation field than in regions closer to the Sun. Color bars are the same for each figure, and are plotted with arbitrary units that are scaled between the minimum and maximum fluxes of 4.0×10^4 and 8.0×10^4 photons cm^{-2} s^{-1} Å^{-1}, respectively.